A review of metal-ion-flux-controlled growth of metastable TiAlN by HIPIMS/DCMS co-sputtering

Grzegorz Greczynski, Jun Lu, Jens Jensen, S. Bolz, W. Koelker, Ch. Schiffers, O. Lemmer, Joseph E Greene and Lars Hultman

Original Publication:

Grzegorz Greczynski, Jun Lu, Jens Jensen, S. Bolz, W. Koelker, Ch. Schiffers, O. Lemmer, Joseph E Greene and Lars Hultman, A review of metal-ion-flux-controlled growth of metastable TiAlN by HIPIMS/DCMS co-sputtering, 2014, Surface & Coatings Technology, (257), , 15-25.
http://dx.doi.org/10.1016/j.surfcoat.2014.01.055

A Review of Metal-ion-flux-controlled Growth of Metastable TiAlN by HIPIMS/DCMS Co-sputtering

G. Greczynski,[1*] J. Lu,[1] J. Jensen,[1] S. Bolz,[2] W. Kölker,[2]
Ch. Schiffers,[2] O. Lemmer,[2] J.E. Greene,[1,3,4] and L. Hultman[1]
[1] Department of Physics (IFM), Linköping University, SE-581 83 Linköping, Sweden
[2] CemeCon AG, Adenauerstr. 20 A4, D-52146 Wűrselen, Germany
[3] Materials Science and Physics Departments and the Frederick Seitz Materials Research Laboratory, University of Illinois, Urbana, Illinois 61801
4 Department of Physics, University of Illinois, Urbana, Illinois 61801, USA

* - corresponding author (grzgr@ifm.liu.se; phone: +46 13 281213)

Abstract

We review results on the growth of metastable $Ti_{1-x}Al_xN$ alloy films by hybrid high-power pulsed and dc magnetron co-sputtering (HIPIMS/DCMS) using the time domain to apply substrate bias either in synchronous with the entire HIPIMS pulse or just the metal-rich portion of the pulse in mixed Ar/N_2 discharges. Depending upon which elemental target, Ti or Al, is powered by HIPIMS, distinctly different film-growth kinetic pathways are observed due to charge and mass differences in the metal-ion fluxes incident at the growth surface. Al^+ ion irradiation during Al-HIPIMS/Ti-DCMS at 500 °C, with a negative substrate bias V_s = 60 V synchronized to the HIPIMS pulse (thus suppressing Ar^+ ion irradiation due to DCMS), leads to single-phase NaCl-structure $Ti_{1-x}Al_xN$ films ($x \leq 0.60$) with high hardness (> 30 GPa with x > 0.55) and low stress (0.2–0.8 GPa compressive). Ar^+ ion bombardment can be further suppressed in favor of predominantly Al^+ ion irradiation by synchronizing the substrate bias to only the metal-ion-rich portion of the Al-HIPIMS pulse. In distinct contrast, Ti-HIPIMS/Al-DCMS $Ti_{1-x}Al_xN$ layers grown with Ti^+/Ti^{2+} metal ion irradiation and the same HIPIMS-synchronized V_s value, are two-phase mixtures, NaCl-structure $Ti_{1-x}Al_xN$ plus wurtzite AlN, exhibiting low hardness (≃18 GPa) with high compressive stresses, up to -3.5 GPa. In both cases, film

properties are controlled by the average metal-ion momentum per deposited atom $\langle p_d \rangle$ transferred to the film surface. During Ti-HIPIMS, the growing film is subjected to an intense flux of doubly-ionized Ti^{2+}, while Al^{2+} irradiation is insignificant during Al-HIPIMS. This asymmetry is decisive since the critical $\langle p_d \rangle$ limit for precipitation of *w*-AlN, 135 $[\text{eV-amu}]^{1/2}$, is easily exceeded during Ti-HIPIMS, even with no intentional bias. The high Ti^{2+} ion flux is primarily due to the second ionization potential (IP_2) of Ti being lower than the first IP (IP_1) of Ar. New results involving the HIPIMS growth of metastable $Ti_{1-x}Al_xN$ alloy films from segmented TiAl targets are consistent with the above conclusions.

Keywords: HIPIMS; HPPMS; TiAlN; ionized PVD

I. Introduction

Metastable NaCl-structure $Ti_{1-x}Al_xN$ alloy films with high hardness and high-temperature oxidation resistance are obtained by physical vapor deposition during kinetically-limited low-temperature growth incorporating dynamic low-energy ion-irradiation-induced mixing in the near-surface region. In conventional dc magnetron sputtering (DCMS), reported AlN kinetic solubility limits in cubic alloys are typically $x_{max} \simeq 0.50$ at film growth temperatures T_s = 500 °C,[1,2] while x_{max} values up to 0.66 have been reported using cathodic arc evaporation[3] with a substrate bias of -100 V.[4] However, both sets of films exhibit extremely high compressive stresses ranging up to -5 GPa for DCMS[5] and -9.1 GPa for arc-deposited films.[6]

There is a large literature on the use of rare-gas ion bombardment of the growing film during low-temperature sputter deposition in order to increase film density,[7,8,9] improve film/substrate adhesion via interfacial mixing,[10,11,12,13] enhance crystallinity and control texture through collisionally-enhanced adatom mean free paths,[14,15,16] form metastable phases through ion-irradiation-induced near-surface mixing,[17,18,19] etc. However, at high ion energies, a steep price is extracted in the form of residual ion-induced compressive stress.[20,21] Early studies of these effects characterized differences in film growth kinetics as a function of the average ion energy per deposited atom $\langle E_d \rangle$.[22,23,24] It was soon realized, however, that $\langle E_d \rangle$, the product of the ion energy E_i and J_i/J_{Me} (the ratio of the accelerated rare-gas ion flux J_i to the deposited metal atom flux J_{Me}) is not a universal parameter for describing the effects of low-energy ion irradiation on film microstructure.[25,16,15] In fact, as first shown for the growth of $Ti_{0.5}Al_{0.5}N$ alloys, ion-irradiation-induced changes in film microstructure, texture, phase composition, and nitrogen ion-to-metal ratio follow distinctly different mechanistic pathways depending upon whether E_i or J_i/J_{Me} is varied, resulting in quite different film properties for the same value of $\langle E_d \rangle$.[25] Clearly,

as is now commonly recognized, the kinetic pathway for optimizing the beneficial effects of rare-gas ion bombardment during film growth while minimizing deleterious effects, is to maintain E_i low (below the lattice displacement threshold, ~ 20-50 eV depending upon the ion and film species involved) while independently increasing J_i/J_{Me} by, for example, magnetically-unbalanced magnetron sputter deposition.[26]

The incident ion energy E_i and ion-to-metal flux ratio J_i/J_{Me} are decisive parameters controlling nanostructural evolution during low temperature (< 500 °C; T_s/T_m < 0.3 for TiN) physical vapor deposition of transition-metal (TM) nitrides by conventional reactive DCMS.[17,25,27,28,29,30,31] The dominant ion species incident at the growth surface during DCMS with N_2/Ar gas mixtures optimized to obtain stoichiometric films is typically Ar^+, with N_2^+ and N^+ both contributing a few percent.[32,33] The N_2^+/N^+ ratio increases with increasing N_2/Ar fraction, while in pure N_2 discharges the dominant ion species is N_2^+.[32] For magnetron sputtering, in which anode sheaths are typically ≤ 1 mm (that is, essentially collisionless), the average energy E_i of ions incident at the growing film is $E_i = E_i^o + ne(V_s - V_{pl})$,[25,27] in which E_i^o denotes the average energy of ions entering the anode sheath, n accounts for the charge state of the ion, and V_{pl} is the plasma potential (typically 3-10 V).[26] E_i^o corresponds to the mean value of the Sigmund-Thompson energy distribution function for sputter-ejected atoms[34] convolved with (i) the probability function for electron impact ionization,[35] and (ii) the probability function for collisions with Ar neutrals between the target and the substrate.

In addition to E_i and J_i/J_{Me}, the average momentum transfer per deposited atom $\langle p_d \rangle = \sqrt{2mE_i} \times J_i/J_{Me}$,[36,37,38] as well as the chemical nature of the ion, inert gas *vs.* metal, are also expected to play an important role in controlling structural evolution. We focus particularly on these latter effects in this review and use, as a model system, metastable TiAlN alloy films with a

phase content which is very sensitive to ion irradiation conditions during growth. In order to exploit this fact, hybrid deposition systems in which high-power pulsed magnetron sputtering (HIPIMS)[39] is combined with a conventional dc magnetron (DCMS) have been employed.[40,41,42,43] Two features of HIPIMS render this technique particularly attractive for growth of metastable TM nitride alloys: (i) the ability to ionize up to 90% (depending upon the metal and power level applied per pulse) of the sputtered metal flux,[44] and (ii) the time separation of metal- and gas-ion fluxes at the substrate.[45] HIPIMS/DCMS co-sputtering has also been investigated for obtaining a higher ionization degree of sputtered species without significant loss of deposition rate.[46,47,48]

In Sec. II, we discuss the results of energy-analyzed mass spectrometry measurements performed to determine ion-energy distribution functions (IEDFs) at the substrate position for Al and Ti targets operated in HIPIMS and DCMS. The distinctly different flux distributions obtained from targets driven in HIPIMS vs. DCMS modes allow the effects of individual metal-ion fluxes, Al^{n+} *vs.* Ti^{n+} (n = 1,2), on film growth kinetics and film properties, to be studied separately.[40] Results for the growth of $Ti_{1-x}Al_xN$ films with AlN-concentrations $0.40 \leq x \leq 0.74$ using different target arrangements, Al-HIPIMS/Ti-DCMS and Ti-HIPIMS/Al-DCMS, are reviewed in Sec. III. Proper selection of the incident metal-ion irradiation (in this case, Al^+ ions in the Al-HIPIMS/Ti-DCMS target configuration) provides the ability to grow fully-dense single-phase cubic $Ti_{1-x}Al_xN$ films with high-AlN concentrations, combining high hardness and low residual stress, all of which are difficult to achieve by either DCMS alone or by cathodic arc deposition. The high flux of Ti^{2+} ions present during Ti-HIPIMS/Al-DCMS is detrimental to the properties of metastable $Ti_{1-x}Al_xN$ alloys; the resulting high momentum transfer to the growing film surface results in precipitation of softer wurtzite-structure AlN grains.

The chemical nature of the incident ion, inert gas *vs.* metal, also plays an important role in controlling film nanostructure evolution. This issue is addressed in Sec. IV using the time domain to apply substrate bias either in synchronous with the entire HIPIMS pulse or just the metal-rich portion of the HIPIMS pulse, during Al-HIPIMS/Ti-DCMS growth of $Ti_{1-x}Al_xN$ films with a fixed composition, $x = 0.61$.[42] Energetic Al^+ ions cause sufficient lattice-atom displacements to eliminate film porosity, and, as opposed to Ar, are primarily incorporated in lattice sites resulting in low residual stress and single-phase films.

The effects of varying metal-ion energy E_i *vs*. momentum p_i on the nanostructure, phase composition, and stress of $Ti_{1-x}Al_xN$ alloys, with $x \simeq 0.6$, are reviewed in Sec. V. Metal-ion energy is varied selectively by applying a bias, ranging from 20 to 280 V, to the substrate in synchronous with the metal-rich part of the HIPIMS pulse, minimizing the effect of concurrent gas-ion bombardment.[43] The phase composition of TiAlN alloy films, and the resulting mechanical properties, are shown to be determined primarily by the average metal-ion momentum transfer per deposited atom $\langle p_d \rangle$. In the case of irradiation with higher-mass film constituents such as Ti, which have a significant concentration of multiply-charged metal ions, $\langle p_d \rangle$ easily exceeds the threshold necessary to cause precipitation of *w*-AlN even when no intentional bias is applied.

In Sec. VI, new results are presented showing that the detrimental role of Ti^{2+} ion irradiation is also evident in the case of $Ti_{1-x}Al_xN$ layers, $0.32 \leq x \leq 0.76$, deposited from single segmented TiAl targets operated in HIPIMS mode. HIPIMS growth of high-AlN-content metastable $Ti_{1-x}Al_xN$ films with high hardness and low residual stress is still possible, but requires precise control of metal ion charge state (1+ *vs*. 2+).

II. Mass and energy analyses of ions incident at the substrate during HIPIMS and DCMS

Knowledge of the mass, flux, and energy distribution of each ion species incident at the film growth surface is essential for establishing the relationship between plasma process parameters and the properties of resulting thin films. In the case of pulsed-plasmas such as HIPIMS, the time evolution of ion fluxes is also important. Thus, we begin with mass and energy analyses in which the spectrometer orifice is placed at the substrate position (target-substrate separation = 18 cm) facing the target. Ion-energy-distribution functions (IEDFs) are plotted in Figure 1 for Al and Ti targets sputtered separately in both HIPIMS and DCMS modes using 1.0:0.2 Ar:N_2 gas mixtures at a total pressure P_{tot} = 0.4 Pa (3 mTorr). Ar flow is set at 350 cm^3/min (sccm), while the N_2 flow is controlled by a feedback loop to maintain P_{tot} constant at 70 sccm. The DCMS data are acquired in time-averaged mode, while the HIPIMS data are obtained in time-resolved mode during the ~20 μs window in which the target current densities are at their maximum values (1.14 A/cm^2 for Ti and 0.39 A/cm^2 for Al). Additional details of the sputtering system, mass spectrometer, and data analysis procedures are given in Ref. 49.

Fig.1 shows that, independent of the target (Al or Ti), sputtering in the DCMS mode yields a continuous flux of low-energy ions, $E_i \simeq 2$ eV, dominated by Ar^+ (~85%) with minor contributions from Al^+ or Ti^+ (6-10%) and N_2^+ (5-8%) ions. In contrast, during HIPIMS pulses, high-intensity fluxes of energetic metal ions are obtained with the metal-ion fraction in the ionized flux bombarding the film surface increasing to ~27% for Al^+ and ~25% for Ti^+/Ti^{2+} ions, comparable to that of Ar^+ ions (27-37%) and larger than for N_2^+ ions (12-22%). The contribution of metal-ions to the total ion flux depends on both the peak target current density J_T and the phase of the high-power pulse, as discussed in Sec. IV. Co-sputtering in a hybrid configuration in which one target is operated in HIPIMS, while the other is operated in DCMS mode, provides an

opportunity to probe the effect of individual energetic metal ion fluxes, Al^{n+} *vs*. Ti^{n+}, on the growth of metastable $Ti_{1-x}Al_xN$ films. Total metal deposition between HIPIMS pulses is $< 2\times10^{-3}$ ML. Thus, newly-deposited film atoms are exposed to incident metal ion irradiation during the subsequent HIPIMS pulse.

A crucial difference between HIPIMS operation of Ti and Al targets is the contribution of doubly-ionized metal-ions. As illustrated in Fig. 2, where the pulse-averaged fraction of doubly-charged metal-ions is plotted as a function of peak target current density J_T during Ti-HIPIMS, an intense flux of Ti^{2+} ions is detected which, depending on J_T, is between 2 and 26% of the total metal-ion flux at the substrate position. However, for Al-HIPIMS, Al^{2+} is < 0.05% of the total metal flux even for J_T as high as 1.5 A/cm^2. Thus, for all values of J_T, the relative contribution of doubly-charged metal-ions is two to three orders of magnitude higher during Ti-HIPIMS. This asymmetry becomes decisive upon application of a moderate substrate bias voltage as discussed in Sec. III.

The primary reason for the large difference in Ti^{2+} *vs.* Al^{2+} fluxes is the correspondingly large difference in second-ionization potentials (IP_2). For HIPIMS plasmas, the primary ionization mechanism is due to electron impact,[35] thus the relative metal and gas IP values are key. The second ionization potential of Al (18.83 eV) is significantly higher than the first IP (IP_1) of Ar (15.76 eV), N_2 (15.55 eV), and N (14.50 eV).[50] In addition, the short plasma transit time of the relatively low-mass sputter-ejected Al atoms (m_{Al} = 26.98 amu) further decreases the probability for multiple ionization events. For sputtered Ti atoms, IP_2 (13.62 eV) is lower than IP_1 of the gas species and the mass (m_{Ti} = 47.88 amu) is higher, thus resulting in higher Ti^{2+} fluxes.

III. Selective control of metal-ion fluxes during growth of TiAlN by HIPIMS/DCMS

A hybrid HIPIMS/DCMS co-sputtering configuration, in which one elemental target (either Ti or Al) is powered by HIPIMS, while the other is operated as a conventional dc magnetron, has been used to grow metastable $Ti_{1-x}Al_xN$ alloy films over a wide composition range ($0.4 \leq x \leq 0.74$).[40,41,42,43] A negative substrate bias , V_s = 60 V, is applied only during HIPIMS pulses to minimize DCMS gas-ion irradiation of the growing film. The position of the substrate is fixed during film growth and the target-to-substrate distance is 180 mm. Switching the positions of Ti and Al target provides the opportunity to investigate the effects of individual energetic metal ion fluxes, Al^{n+} *vs*. Ti^{n+}, incident at the growth surface during HIPIMS pulses. In the Al-HIPIMS/Ti-DCMS configuration, the average power to the Al HIPIMS target is 2.5 kW (5 J/pulse, 500 Hz, 10% duty cycle, limited by arcing in reactive mode), resulting in a peak target current density of 0.41 A/cm^2. For experiments carried out in the Ti-HIPIMS/Al-DCMS configuration, a higher average HIPIMS power, 5 kW (10 J/pulse, 500 Hz, 10% duty cycle), is necessary in order to obtain films in the desired composition range since the Ti sputtering rate is approximately half that of Al. The resulting peak target current density is 1.34 A/cm^2. The choice of target current densities has no influence on the key difference between Al-HIPIMS and Ti-HIPIMS; that is, a lack of doubly-ionized metal-ions in the former case, as evident from Figure 2.

Figure 3 shows two sets of θ-2θ scans, obtained with Cu Kα radiation (1.5406 Å) as a function of the sample tilt angle ψ (defined as the angle between the surface normal and the diffraction plane containing the incoming and diffracted x-ray beams), varied from 0° to 75° in steps of 5°, for $Ti_{0.41}Al_{0.59}N$ alloys grown using (a) Al-HIPIMS/Ti-DCMS and (b) Ti-HIPIMS/Al-DCMS. Despite the relatively high AlN concentration, x = 0.59, films grown in the Al-HIPIMS/Ti-DCMS configuration (Fig. 3(a)) are single phase, with the NaCl structure.

Diffraction peak positions measured at $\psi = 35°$ (close to the strain-free tilt angle ψ^*)[51] exhibit large shifts toward higher 2θ angles ($2\theta_{002} = 43.36°$), with respect to reference TiN powder patterns ($2\theta_{002} = 42.60°$),[52] indicative of the incorporation of AlN into the cubic TiN lattice. In contrast, Ti-HIPIMS/Al-DCMS films with the same composition (Fig. 3(b)) consist of a mixture of cubic and wurtzite AlN phases, with volume fractions, estimated from *w*-AlN $10\bar{1}0$ and *c*-TiN 002 XRD peaks intensities integrated over all ψ angles and normalized to integrated powder diffraction values, of 47% cubic and 53% wurtzite.

The much lower diffracted peak intensities in Figure 3(b) compared to 3(a) is indicative of smaller average grain sizes for Ti-HIPIMS/Al-DCMS films. The relaxed cubic lattice parameter a_o of $Ti_{0.41}Al_{0.59}N$ Al-HIPIMS/Ti-DCMS films is 4.170 Å; while that of Ti-HIPIMS/Al-DCMS layers with the same composition is 4.213 Å. Thus, XRD results reveal markedly different film growth pathways for Al-HIPIMS/Ti-DCMS *vs*. Ti-HIPIMS/Al-DCMS leading to a significantly higher AlN kinetic solid-solubility limit for films grown in the Al-HIPIMS/Ti-DCMS configuration.

The above conclusions are corroborated by typical XTEM images shown in Figure 4, with corresponding selected-area electron diffraction (SAED) patterns, of (a) a $Ti_{0.47}Al_{0.53}N$ layer grown in the Ti-HIPIMS/Al-DCMS configuration and (b) a $Ti_{0.41}Al_{0.59}N$ film grown by Al-HIPIMS/Ti-DCMS. Both samples exhibit dense columnar structures with no open boundaries and an average column diameter of 30±10 nm. Despite a lower AlN concentration, $x = 0.53$, the SAED pattern from the Ti-HIPIMS/Al-DCMS film contains both cubic (111, 002, and 022) and wurtzite (0002 and $10\bar{1}0$) diffraction rings. In contrast, the SAED pattern obtained from the $x = 0.59$ layer grown under periodic Al^+ bombardment from the Al-HIPIMS target, contains only

NaCl-structure diffraction rings (111, 002, and 022) indicating a single-phase film despite a higher AlN concentration (hence, a larger driving force for decomposition).

The dependence of phase composition on target configuration is directly related to film mechanical properties as shown in Fig. 5, for which the nanoindentation hardness H and residual stress values σ obtained from $\sin^2\psi$ analyses of all $Ti_{1-x}Al_xN$ films are plotted as a function of AlN concentration for the two target configurations. Hardness values of both Al-HIPIMS/Ti-DCMC and Ti-HIPIMS/Al-DCMS films are approximately the same for $x \sim 0.4$ ($H \simeq 24$ GPa) and for $x \sim 0.67$ ($H \simeq 19$ GPa). However, over the intermediate AlN concentration range, $0.40 < x < 0.67$, $H(x)$ exhibits a strong dependence on target configuration. For Al-HIPIMS/Ti-DCMS $Ti_{1-x}Al_xN$ layers, H increases with x reaching a maximum value of ~30 GPa with $0.55 \leq x \leq 0.60$ and then decreases rapidly at higher x values to ~20 GPa. In contrast, $H(x)$ for Ti-HIPIMS/Al-DCMS films decreases to ~19 GPa with $x > 0.4$ and then remains approximately constant throughout the remaining concentration range.

Films stress *vs*. concentration ($\sigma(x)$) results, corrected for differential thermal contraction σ_{th} due to the samples being cooled from T_s = 500 °C to room temperature, also exhibit large differences between Al-HIPIMS/Ti-DCMS and Ti-HIPIMS/Al-DCMS $Ti_{1-x}Al_xN$ films with similar compositions: while Al-HIPIMS/Ti-DCMS alloys have low compressive stresses, varying from -0.2 GPa with x = 0.43 to -1.3 GPa with x = 0.64, Ti-HIPIMS/Al-DCMS films have large compressive stresses, from -2.1 to -3.5 GPa, over the entire composition range.

Single-phase $Ti_{1-x}Al_xN$ alloy films with high AlN concentrations, $0.55 \leq x \leq 0.60$, and grown in the Al-HIPIMS/Ti-DCMS mode, combine high hardness (H = 30 GPa) with low residual stress (~ -0.8 GPa), a set of properties difficult to achieve by either DCMS alone or by

cathodic arc deposition, for which high H values are typically the result of high compressive stress which can range from -3.1 (ref. 3) to -9.1 GPa.[6] For DCMS and cathodic arc films, both H and σ decrease during post-annealing[53] (or during elevated-temperature applications such as high-speed machining) as residual point defects are annealed out. This does not occur with the Al-HIPIMS/Ti-DCMS $Ti_{1-x}Al_xN$ films. In fact, upon post-deposition annealing at 900 °C, $Ti_{0.41}Al_{0.59}N$ film hardness actually increases to 33 GPa due to the formation of coherent cubic AlN via spinodal decomposition.[41]

The results achieved during Al-HIPIMS/Ti-DCMS deposition are attributed to a combination of kinetically-limited growth and dynamic near-surface mixing, the latter due predominantly to Al^+ and Ar^+ ion irradiation during HIPIMS pulses. The lack of multiply-charged metal ions during Al-HIPIMS/Ti-DCMS deposition means that the average ion energy incident at the film surface during HIPIMS pulses ranges from ~62 (Ar^+ ions) to ~72 eV (Al^+ ions) which together with the time-averaged ion-to-metal flux ratio J_i/J_{Me} of 2.5±0.5,[40] gives rise to effective near-surface ion mixing, thereby inhibiting the precipitation of wurtzite AlN second phases, without significant residual ion damage. This, in turn, enables solid-solution hardening; $H(x)$ increases from 24 GPa with x = 0.40 to 30 GPa with x = 0.59. Elastic moduli (not shown) range from 350 to 410 GPa. However, with increasing x, the mixing enthalpy also increases and, at x > 0.65 the driving force towards decomposition overcomes dynamic near-surface ion mixing effects and wurtzite-structure AlN precipitates out of solution.

In contrast, with Ti-HIPIMS/Al-DCMS, two-phase $Ti_{1-x}Al_xN$ films are obtained at all compositions. The layers exhibit low hardness with high compressive stress. This dramatic difference in film properties compared to Al-HIPIMS/Ti-DCMS is primarily due to the presence of an intense flux of doubly-ionized Ti^{2+} ions ($J_{Ti^{2+}}/J_{Ti^+}$ = 0.42 during the most energetic phase of

the high-power pulse), with a mean ion energy greater than 140 eV due to the 2× energy gain of doubly-charged ions under the applied substrate bias, V_s = 60 V. The resulting momentum transfer per deposited atom (see Section V) is more than enough for creation of the high density of residual defects[17,54] observed as speckle contrast in XTEM images and explains the high compressive stress. The defects also serve as nucleation centers for the formation of wurtzite-structure AlN precipitates. As a consequence, both *H* and *E* are low, with values close to that of hexagonal AlN, whereas the residual stress is high (2.1-3.5 GPa).

Overall, the results clearly demonstrate that the use of combined HIPIMS/DCMS co-sputtering provides enhanced flexibility in tuning the microstructure and physical properties of as-deposited alloy films.

IV. Synchronous substrate biasing to probe effects of gas-ion *vs.* metal-ion irradiation during Al-HIPIMS/Ti-DCMS

The results presented in the previous section demonstrated that the type of metal-ion irradiation during film growth plays a crucial role in determining film microstructure, phase content, and mechanical properties of $Ti_{1-x}Al_xN$ model alloys. In addition to effects related to the use of different metal-ion fluxes (Al^+ *vs*. Ti^+/Ti^{2+}), the chemical nature of the incident ion, inert gas *vs.* metal, also plays an important role in controlling film microstructural evolution.[42]

Ion fluxes -- Ar^+, N_2^+, N^+, and Al^+ -- incident at the growing film during Al-HIPIMS/Ti-DCMS are shown, with 20 μs resolution, in the upper-left panel of Fig. 6.[42] Each data point at time *t* represents the corresponding ion fluxes collected during the interval from *t*-10 to *t*+10 μs. For Al-HIPIMS in Ar/N_2 mixtures,[42] the plasma is initially maintained primarily by Ar^+ and N_2^+ gas ions. The ~20 μs time delay before the appearance of atomic N^+ ions, together with the high

N^+ mean energy (relative to N_2^+ ions), indicates that they originate primarily from N atoms sputter ejected from the target surface and ionized in the plasma.

Gas-ion intensities begin to decrease after 30-40 μs. This occurs for two reasons: (i) gas rarefaction stemming from the high thermal and momentum load supplied by the HIPIMS target,[49,55] and (ii) the fact that the ionization probability of gas species Ar, N_2, and N with high IP_1 values (15.75, 15.55, and 14.50 eV, respectively)[50] decreases due to an intense flux of sputtered Al atoms with low IP_1 (5.986 eV), whose ionization reduces the average electron energy and the intensity of the high-energy tail in the plasma electron energy distribution. As a consequence, from $t \simeq$ 40-100 μs into the pulse, Al^+ is the dominant plasma ion.

The Al^+ intensity, after reaching a peak at ~50 μs, begins to decrease due to a corresponding decrease in the discharge current as the plasma becomes power-supply limited. The Ar^+ intensity again dominates during the latter half of the pulse, from $t \simeq$ 100-200 μs. N_2^+ and N^+ intensities do not fully recover due to increased target sputtering rates giving rise to efficient trapping and chemisorption of nitrogen by freshly-deposited Al atoms.

The existence of the metal-ion-dominated phase during high-power pulses, illustrated in Fig. 6, provides an opportunity to separate metal-ion from gas-ion-induced effects on the microstructure and properties of metastable $Ti_{1-x}Al_xN$ alloys. This is realized by synchronizing the substrate bias during film growth by hybrid HIPIMS/DCMS co-sputtering.[42] A 60 V negative substrate bias is applied using three different approaches: (1) the bias is continuous during both HIPIMS pulses and DCMS (100% duty cycle), (2) the bias is applied in synchronous with the full HIPIMS pulse (10% duty cycle), and (3) the bias is applied in synchronous with the metal-rich-plasma portion of the HIPIMS pulse (3% duty cycle). For the remaining deposition time, in modes (2) and (3), the growing films are at (negative) floating potential $V_f \simeq$ 10 V.

Oscilloscope wave forms, corresponding to all three bias scenarios, are shown in Fig. 6 together with typical XTEM images and SAED patterns obtained from corresponding Al-HIPIMS/Ti-DCMS $Ti_{0.39}Al_{0.61}N$ films. Fig. 6(a) reveals that mode (1) films consist of small grains (~200×200-500 $Å^2$) throughout the film thickness, elongated along the growth direction. This structure results from recurring renucleation due to (i) residual damage from intense Ar^+ ion bombardment and (ii) the precipitation of incoherent *w*-AlN phase grains, both of which interrupt local epitaxy. The SAED pattern consists of cubic $Ti_{1-x}Al_xN$ 111, 002, and 022, and wurtzite AlN 0002 and $10\bar{1}0$, diffraction rings. The uniform angular intensities of the diffracted signals are indicative of random grain orientation. Intense Ar^+ ion irradiation during mode (1) growth also results in extensive material loss by resputtering, predominantly during the DCMS phase, leading to thinner films, 1.2 μm, for a deposition time of 90 min. The presence of residual trapped Ar, 0.2 at%, and ion-induced defects explain the observed high compressive stress, -4.6 GPa,[42] in which differential thermal contraction stress, 1.6 GPa, upon cooling the sample from T_s, has been accounted for.

The nanostructure of mode (2) $Ti_{0.39}Al_{0.61}N$ layers, deposited using synchronized t = 0-200 μs pulsed bias (see Fig. 6(b)), is similar to that of mode (1) films, but with a larger grain size. Since there is no applied bias between HIPIMS pulses, resputtering is reduced, and thicker films (1.9 μm) are obtained. The correspondingly lower defect densities result in a lower renucleation rate; hence, the average grain size is larger (~300×1000-1500 $Å^2$) and more elongated in the growth direction. The volume fraction of *w*-AlN second phase precipitates is considerably decreased as revealed by a very weak (compared to mode (1) films) *w*-AlN 0002, and no observable $10\bar{1}0$, ring. The incorporated Ar concentration is below detection limits (< 0.1 at%) and the residual stress is lower, -1.8 GPa.

A very different nanostructure is observed for mode (3) films (see Fig. 6(c)) grown with the substrate bias synchronized to the metal-ion portion of the HIPIMS pulse (t = 40-100 μs). In this mode, concurrent Ar^+, N_2^+, and N^+ gas-ion bombardment is minimized during the 60-μs bias pulses; the majority of gas ions arrive at the substrate during the dc-phase when no intentional bias is applied. As a consequence, the $Ti_{0.39}Al_{0.61}N$ layers are single-phase NaCl-structure with no wurtzite signal detectable by SAED. Above an initial competitive-texture zone (~200 Å), local epitaxy is uninterrupted and the films consist of densely-packed columns, with no open boundaries, that extend throughout the remaining film thickness, 1.9 μm. Al^+ irradiation results in sufficient lattice atom displacements (through recoils and forward momentum transfer in shallow overlapping cascades) to eliminate the voids typically observed in low-temperature ($T_s/T_m \leq 0.3$) TM nitride films.[17,25,28,30,31] The average column diameter, ~200 Å near the substrate, increases to 600-700 Å by the middle of the film, and 700-1000 Å near the film surface.

During the early stages of mode (3) growth, films exhibit a randomly oriented, fine-grain equiaxed structure (~200×200 $Å^2$) consisting of approximately equal volume fractions of 002 and 111 oriented grains, from which, unlike layers grown in modes (1) and (2), a kinetically-limited 111 preferred orientation evolves. Adatom residence times are longer on the low-potential-energy, low-diffusivity 111 surfaces, thus the local 111 epitaxial growth is preserved.[27,30,56] The residual defect concentration, and hence residual stress (-0.9 GPa), is lower under Al^+ rather than Ar^+ ion irradiation since Al is primarily incorporated into the lattice of the growing film, whereas Ar resides in interstitial sites.

Thus, applying a bias synchronized with the metal-ion-rich portion of the HIPIMS pulse opens a new pathway for control of microstructure evolution, allowing low-temperature growth

of single-phase metastable alloys with larger grain size, strong preferred orientation, high hardness, and low stress.

V. Metal-ion energy *vs*. metal-ion momentum effects during $Ti_{0.4}Al_{0.6}N$ HIPIMS/DCMS

The effects of time-averaged Ti^+/Ti^{2+} *vs*. Al^+ metal-ion energy $\langle E_d \rangle$ and momentum $\langle p_d \rangle$ per deposited atom on metastable $Ti_{1-x}Al_xN$ film microstructure, phase composition, and residual stress have been investigated using hybrid HIPIMS/DCMS co-sputter deposition.[43] Sets of $Ti_{1-x}Al_xN$ alloy films, with $x \simeq 0.6$, were grown from Ti and Al targets in Al-HIPIMS/Ti-DCMS and Ti-HIPIMS/Al-DCMS configurations.[40] Energy and momentum transfer due to gas-ion bombardment was minimized by synchronizing the substrate bias to the metal-ion-rich portion of the HIPIMS pulse, and the effects of Ti and Al ion energy and momentum probed by varying the amplitude of the negative bias V_s, from 20 to 280 V. Alloy film stoichiometry is independent of V_s, as determined by ERDA, due to the very low duty cycle (3%) of the synchronized bias pulses. The time-averaged metal-ion to neutral metal flux ratios $\langle J_i/J_{Me} \rangle$, for which J_i was determined using flat probes at the substrate position during film growth, are 2.5 for Al-HIPIMS/Ti-DCMS and 5.4 for Ti-HIPIMS/Al-DCMS layers.[43]

Figures 7(a) and 7(b) are XTEM images of Al-HIPIMS/Ti-DCMS and Ti-HIPIMS/Al-DCMS $Ti_{1-x}Al_xN$ multilayers grown as a function of V_s with the thickness of each individual layer ~200 nm. For Al-HIPIMS/Ti-DCMS multilayers, V_s was increased from 20 to 80 V in steps of 20 V, and thereafter in steps of 40 V up to a maximum value of 280 V. V_s was varied in the same sequence for Ti-HIPIMS/Al-DCMS multilayers, except that the maximum value was V_s = 120 V since single-layer films spontaneously delaminated, due to extremely high compressive stress, at higher substrate bias. Selected-area electron diffraction (SAED) patterns obtained with the

aperture set to sample the entire layer thickness are also shown. Clearly, there are significant V_s -dependent differences in film microstructure evolution between layers obtained with the two target configurations. The type of metal-ion incident at the substrate plays a critical role in determining the phase composition of as-deposited films. Al-HIPIMS/Ti-DCMS layers grown under relatively low mass (26.98 amu) singly-ionized Al^+ irradiation exhibit a dense columnar structure with average column diameters ranging from 40 nm with V_s = 20 V to 90 nm with V_s = 240 V (see Fig. 7(a)). For Al-HIPIMS/Ti-DCMS films grown with $V_s \leq 160$ V, the columns are predominantly single grains while at higher bias voltages, $V_s \geq 200$ V, local epitaxy is interrupted due to highly energetic ion bombardment giving rise to renucleation leading to columns composed of smaller crystallites, as evident from SAED patterns. The speckle contrast observed in $V_s \geq 200$ V Al-HIPIMS/Ti-DCMS films indicates the presence of high densities of point defect complexes which serve as preferential nucleation sites for second-phase *w*-AlN precipitates. Al-HIPIMS/Ti-DCMS TiAlN layers grown with $V_s \leq 160$ V are all single-phase NaCl-structure alloys.

The use of higher mass (47.88 amu) Ti^+/Ti^{2+} ion irradiation during growth of Ti-HIPIMS/Al-DCMS films yields results which are in strong contrast. XTEM images of Ti-HIPIMS/Al-DCMS multilayers show (see Fig. 7(b)) that local epitaxy in single columns is interrupted even at the lowest bias, V_s = 20 V. The columns in these films are narrow, $\langle d \rangle$ = 15-25 nm, and consist of small, randomly-oriented intracolumnar grains indicative of continuous renucleation. Both XRD and SAED results clearly indicate that all Ti-HIPIMS/Al-DCMS films are two-phase mixtures of NaCl-structure TiAlN and hexagonal *w*-AlN.

Figure 8(a) is a plot of the average metal-ion energy deposited per atom, $\langle E_d \rangle = \langle J_i / J_{Me} \rangle E_i \xi_i$, where ξ_i are metal-ion contributions to the total ion flux, as a function of

V_s during Al-HIPIMS/Ti-DCMS and Ti-HIPIMS/Al-DCMS. $\langle E_d \rangle_{Ti^+/Ti^{2+}}$ is greater than $\langle E_d \rangle_{Al^+}$ by factors which range from 2.7 to 3.3 as V_s is increased from 20 to 120 V. This is due to both the higher time-averaged Ti^+/Ti^{2+} ion current and the 2× higher acceleration energy of doubly-charged Ti^{2+} ions. However, this difference in $\langle E_d \rangle$ for Al-HIPIMS *vs.* Ti-HIPIMS is not sufficient to account for the observed changes in $Ti_{1-x}Al_xN$ microstructure and phase content. Ti-HIPIMS/Al-DCMS layers grown with V_s = 20 V ($\langle E_d \rangle_{Ti^+/Ti^{2+}} \simeq$ 130 eV) are two-phase mixtures, *c*-$Ti_{1-x}Al_xN$ and *w*-AlN, with narrow columns, $\langle d \rangle$ = 20±5 nm, and fine intracolumnar grain size. This is in contrast to $Ti_{0.38}Al_{0.62}N$ Al-HIPIMS/Ti-DCMS films deposited with V_s = 80 V, also corresponding to $\langle E_d \rangle_{Al^+} \simeq$ 130 eV, which consist of single-phase NaCl-structure crystallites, with $\langle d \rangle \simeq$ 60±5 nm, in a dense columnar microstructure in which each column is a single extended grain. Precipitation of second-phase *w*-AlN grains during Al-HIPIMS/Ti-DCMS growth requires $V_s \geq$ 200 V, corresponding to $\langle E_d \rangle_{Al^+} \simeq$ 300 eV. Thus, the physical properties of Al-HIPIMS/Ti-DCMS and Ti-HIPIMS/Al-DCMS $Ti_{1-x}Al_xN$ alloys with similar AlN concentrations and $\langle E_d \rangle$ values are dramatically different. Clearly, $\langle E_d \rangle$ alone does not control the film microstructure and properties during hybrid HIPIMS/DCMS deposition.

The average metal-ion momentum transfer per deposited atom $\langle p_d \rangle$ -- the product of $\langle J_i/J_{Me} \rangle$, the mean metal-ion momentum p_i and ξ_i -- is plotted in Fig. 8(b) as a function of V_s for Al-HIPIMS/Ti-DCMS and Ti-HIPIMS/Al-DCMS films. XRD, TEM, XTEM, and SAED results reveal that all Al-HIPIMS/Ti-DCMS layers grown with $\langle p_d \rangle_{Al^+} \leq \langle p_d^* \rangle$ = 135 [eV-amu]$^{1/2}$, corresponding to $V_s \leq$ 160 V, are single-phase with a NaCl cubic structure. Film growth with $\langle p_d \rangle_{Ti^+/Ti^{2+}} \leq \langle p_d^* \rangle$ translates, in the case of Ti-HIPIMS/Al-DCMS, to $V_s \leq$ 8 V. However, the

negative floating potential during the HIPIMS pulse is ~20 V. Thus, *all* Ti-HIPIMS/Al-DCMS alloys contain *w*-AlN precipitates.

The microstructure and phase content of Al-HIPIMS/Ti-DCMS and Ti-HIPIMS/Al-DCMS films grown under conditions that result in the same $\langle p_d \rangle$ value are quite similar. For example, $\langle p_d \rangle_{Ti^+/Ti^{2+}}$ during Ti-HIPIMS/Al-DCMS film growth with the lowest bias, V_s = 20 V, is ~166 [eV-amu]$^{1/2}$, which corresponds to $V_s \simeq 240$ V during Al-HIPIMS/Ti-DCMS. XTEM and SAED results (see Fig. 7) indicate that the microstructure and phase content of V_s = 20 V Ti-HIPIMS/Al-DCMS and V_s = 240 V Al-HIPIMS/Ti-DCMS alloys are essentially the same. Both layers contain *c*-TiAlN and *w*-AlN grains and exhibit similar average cubic crystallite size. Overall, phase composition, nanostructure, and TiAlN film properties are predominantly controlled by $\langle p_d \rangle$, rather than $\langle E_d \rangle$, during HIPIMS/DCMS film growth.

For singly-charged lower-mass Al^+ metal ions, with IP_2 higher than IP_1 of the sputtering gas, $\langle p_d \rangle$ is a slowly-increasing function of substrate bias (solid curve in Fig. 8(b)) which allows access to low $\langle p_d \rangle$ values not accessible during growth with irradiation by heavier multiply-charged Ti^{2+} metal ions, and provides the opportunity to tune momentum transfer to the growing film surface. Thus, by controlling the amplitude of the synchronous bias pulse applied during the metal-ion portion of the Al-HIPIMS pulse, cubic single-phase metastable $Ti_{0.38}Al_{0.62}N$ films can be obtained with high AlN concentrations, high hardness, and essentially no residual stress. The same procedure should be applicable to other alloy systems composed of high-mass metal constituents with low IP_2 values compared to IP_1 of the sputtering gas (e.g., Zr, Sc, V, Y, Nb, Hf, or Ta) and low mass constituents with high IP_2 values (e.g., Al or Si).

VI. $Ti_{1-x}Al_xN$ films grown from segmented TiAl targets by HIPIMS

In this section, we extend previous investigations to pure HIPIMS growth of metastable $Ti_{1-x}Al_xN$ films from TiAl segmented targets for which competition between Ti^+/Ti^{2+} and Al^+ ion irradiation effects are expected to play an important role. The segmented TiAl target is composed of equal-sized triangular Ti and Al pieces forming a rectangular plate which is the same size as the elemental targets used in the hybrid HIPIMS/DCMS experiments. Total pressure, Ar and N_2 partial pressures, and film growth temperature T_s are the same as in Sec.III, in order to facilitate direct comparison to layers obtained by Al-HIPIMS/DCMS and Ti-HIPIMS/Al-DCMS co-sputtering. $Ti_{1-x}Al_xN$ alloy films with $0.32 \leq x \leq 0.76$ are grown combinatorially in a single run with several small Si(001) substrates placed at different locations, but at the same target-to-substrate distance. The segmented target is powered by HIPIMS (TiAl-HIPIMS) with an average power of 2.5 kW (5 J/pulse, 500 Hz, 10% duty cycle); a negative substrate bias V_s = 60 V is applied synchronously with the HIPIMS pulses.

The metal-ion flux composition from the segmented target varies as a function of position at the substrate platen. Thus, in order to provide a comparison with results for single targets in Section III, mass spectrometry following the procedure described in Sec. II, was used to analyze ion fluxes from an $Ti_{0.3}Al_{0.7}$ alloy target, incident at the center of the platten. HIPIMS was carried out in pure Ar, to avoid overlap between Al^{2+} and N^+ signals, at peak target current density J_T = 1 A/cm^2. Data recorded in time-averaged mode are presented in Figure 9. Multiple peaks Al^+, Ti^+, and Ti^{2+} are due to isotopes. Similar to the observations from elemental Ti and Al targets powered by HIPIMS (see discussion in Sec.III), a very high Ti^{2+} metal-ion flux is detected, while the intensity of the Al^{2+} flux is two orders of magnitude lower despite the much higher Al content in the $Ti_{0.3}Al_{0.7}$ target and an Al sputtering yield which is a factor of 2× higher than that of Ti. This has direct implications for film growth from the segmented TiAl target. Relatively high Ti^{2+}

ion fluxes are obtained even during growth of $Ti_{1-x}Al_xN$ alloy films with higher x values for which the Al metal flux exceeds that of Ti.

Figure 10 shows θ–2θ scans obtained as a function of tilt angle ψ varied from 0° to 75° in steps of 5° for a TiAl-HIPIMS $Ti_{1-x}Al_xN$ alloy with x = 0.62. The film consists of a mixture of cubic and wurtzite AlN phases, with volume fractions, estimated from TiN(002) and AlN($10\bar{1}0$) peak intensities integrated over all tilt angles and normalized to random powder diffraction values, of 8% cubic and 92% wurtzite. The diffraction peaks from the wurtzite phase are clearly shifted toward lower diffraction angles with respect to reference AlN powder patterns[52] independent of the tilt angle ψ, indicating incorporation of TiN into the hexagonal lattice. The later finding confirms the relatively few reports on the subject.[57,58] Relaxed lattice parameters determined from the positions of AlN(0002) and AlN($10\bar{1}0$) peaks measured at ψ = 35°, close to the strain-free tilt angle ψ^* (Ref. 51), are a_o = 3.188 Å and c_o = 5.150 Å, which corresponds to 2.5% and 3.4% linear expansion, respectively. Peaks of the cubic phase are shifted toward higher diffraction angles as a result of lattice contraction due to AlN incorporation into the cubic TiN lattice ($2\theta_{002}$ = 43.16° *vs*. 42.60° for TiN). For comparison, Fig. 3(b) shows that films with essentially the same composition grown by Al-HIPIMS/Ti-DCMS are single-phase cubic.

$Ti_{1-x}Al_xN$ cubic-phase relaxed lattice parameters a_o, obtained directly from $2\theta_{002}$ peak positions recorded at the strain-free tilt angles, are plotted as a function of x for TiAl-HIPIMS together with results for Al-HIPIMS/Ti-DCMS and Ti-HIPIMS/Al-DCMS layers in Figure 11. Only alloy films with sufficient volume fraction (> 5%) of the cubic phase to yield reliable results are included in this comparison. $a_o(x)$ for single-phase TiAl-HIPIMS cubic $Ti_{1-x}Al_xN$ alloys decreases gradually from 4.232 Å with x = 0.32 to 4.184 Å with x = 0.58 following the predictions of density functional theory (DFT) calculations.[59] $a_o(x)$ remains constant for $x \geq 0.58$

due to precipitation of second-phase wurtzite AlN. The XRD AlN solubility limit $x_{max}^{TiAl-HIPIMS}$ extrapolated from the saturation value of $a_o(x)$ is ~0.53,[60] which is close to that of DCMS alloy films, for which reported XRD x_{max} values are ~0.50 at T_s = 500 °C.[1,2]

$a_o(x)$ values for Ti-HIPIMS/Al-DCMS films with $0.41 \leq x \leq 0.66$ are nearly constant at 4.213 Å, with an XRD kinetic AlN solubility limit $x_{max}^{Ti-HIPIMS/Al-DCMS} \leq 0.40$. $a_o(x)$ values for Al-HIPIMS/Ti-DCMS alloys with $x \geq 0.55$ are much lower than either TiAl-HIPIMS or Ti-HIPIMS/Al-DCMS, indicative of higher AlN solubility in the cubic TiN lattice. After a monotonic decrease in $a_o(x)$ with $0.55 \leq x \leq 0.64$, a_o saturates at 4.160 Å for $x \geq 0.65$. Thus, $x_{max}^{Al-HIPIMS/Ti-DCMS}$ is ~0.64.

The $a_o(x)$ XRD results presented in Fig. 11 reveal that the trends for $Ti_{1-x}Al_xN$ alloy films grown from segmented targets constitute an intermediate case between Ti-HIPIMS/Al-DCMS and Al-HIPIMS/Ti-DCMS.

Nanoindentation hardness $H(x)$ results for TiAl-HIPIMS $Ti_{1-x}Al_xN$ alloy films are consistent with the above $a_o(x)$ trends. H initially increases from 25.6 GPa with x = 0.32 to 31.3 GPa with x = 0.43 and then slowly decreases thereafter to 28.5 GPa with x = 0.50 and 21.4±0.6 GPa with $x \geq 0.58$. The AlN concentration range for which $H(x)$ exhibits the largest drop, from 28.5 GPa with x = 0.50 to 21.8 GPa with x = 0.58, corresponds well with the $x_{max}^{TiAl-HIPIMS}$ value of 0.53 obtained from Fig. 11, indicating that the rapid decrease in hardness is associated with the formation of a sufficient volume fraction of wurtzite AlN second phase to be detected by XRD. Comparison with $H(x)$ data in Fig. 5(a) for Al-HIPIMS/Ti-DCMS and Ti-HIPIMS/Al-DCMS $Ti_{1-x}Al_xN$ films reveals that $H(x)$ softening for TiAl-HIPIMS layers occurs at AlN concentrations which are higher than for Ti-HIPIMS/Al-DCMS and lower than for Al-HIPIMS/Ti-DCMS alloys.

TiAl-HIPIMS $Ti_{1-x}Al_xN$ residual stress values $\sigma(x)$ are compressive and increase initially from 2.8 GPa with x = 0.32 to 4.0 GPa with x = 0.43 to reach a maximum of 4.1 GPa with x = 0.50 and decrease thereafter to 2.3 and 1.8 GPa with x = 0.58 and 0.61, respectively. Thus, TiAl-HIPIMS $\sigma(x)$ is significantly higher than for corresponding Al-HIPIMS/Ti-DCMS films and comparable to that of Ti-HIPIMS/Al-DCMS alloy layers (see Fig. 5(b)).

The AlN XRD solubility limit $x_{max}^{TiAl-HIPIMS}$ is higher than $x_{max}^{Ti-HIPIMS/Al-DCMS}$ (0.53 *vs.* $\leq$ 0.40). We attribute this predominantly to the fact that the peak target current density J_T during TiAl-HIPIMS operation is lower than for Ti-HIPIMS/Al-DCMS (0.41 A/cm^2 *vs.* 1.34 A/cm^2) leading to: (i) a lower ionization degree of sputtered species and, (ii) a lower fraction of Ti^{2+} in the ion flux to since for HIPIMS, doubly-charged Ti^{2+} metal ion flux is an increasing function of J_T.[61,62,63]

The hardness of TiAl-HIPIMS $Ti_{1-x}Al_xN$ alloy films with $0.38 \leq x \leq 0.50$ is significantly higher than for corresponding Ti-HIPIMS/Al-DCMS layers as a consequence of high compressive stresses ($3.5 \leq \sigma \leq 4.1$ GPa). Evidence for this comes from TiAl-HIPIMS $Ti_{0.57}Al_{0.43}N$ post-annealing experiments in which H decreases from 31.3 to 25.1 GPa as residual point defects are annealed out during 2 h at 900 °C in an Ar atmosphere. In contrast, annealing Al-HIPIMS/Ti-DCMS $Ti_{0.41}Al_{0.59}N$ films under the same conditions results in an increase in H from 30 to 33 GPa,[41] due to the formation of coherent cubic AlN via spinodal decomposition following the reaction path c-(Ti,Al)N $\rightarrow$ c-TiN + c-AlN.

Mechanical properties of TiAl-HIPIMS alloys are better than those of Ti-HIPIMS/Al-DCMS, but not as good as for Al-HIPIMS/Ti-DCMS layers of the same composition. These results present additional evidence for the detrimental role of energetic Ti^{2+} ions during Ti-

HIPIMS and TiAl-HIPIMS operation. High-AlN-content metastable $Ti_{1-x}Al_xN$ films with high hardness and low residual stress are only obtained in the Al-HIPIMS/Ti-DCMS configuration.

VII. Conclusions

Investigations of hybrid HIPIMS/DCMS deposition, in which metastable $Ti_{1-x}Al_xN$ alloy films are used as a model materials system for which the phase content is sensitive to ion irradiation, show that markedly different film-growth kinetic pathways are obtained depending upon which target (Ti or Al) is powered by HIPIMS. This is due to distinct differences in the average mass, charge, and energy of the metal-ion fluxes incident at the growth surface. During Al-HIPIMS/Ti-DCMS, the Al^{2+} flux is negligible (predominantly due to the high IP_2 value of Al with respect to Ar IP_1) and the film microstructure is primarily controlled by Al^+ and Ar^+ ion irradiation during HIPIMS pulses. Alloys grown in this mode have an XRD kinetic solid-solubility limit of x = 0.64 and combine high hardness, H ~ 30 GPa, (due to solid-solution hardening) with low residual stress, $\sigma \simeq$ -0.8 GPa, a combination of properties which is difficult to achieve by other PVD methods. In sharp contrast, with Ti-HIPIMS/Al-DCMS, $Ti_{1-x}Al_xN$ films are two-phase (cubic plus wurtzite) for x > 0.40. Moreover, the layers exhibit low hardness, H ~18 GPa, with high compressive stress, σ = -3.5 GPa. The dramatic difference in film properties is due to the presence of an intense flux of doubly-ionized Ti^{2+} ions during the Ti-HIPIMS pulses. This is primarily a result of the IP_2 value of Ti being lower than IP_1 for Ar. Large Ti^{2+} fluxes result in high values of incident metal-ion energy $\langle E_d \rangle$ and momentum transfer $\langle p_d \rangle$ per deposited metal atom and give rise to the creation of the residual point defects, formation of relatively soft wurtzite-structure AlN second-phase precipitates and, as a consequence, poor mechanical properties.

In addition to the choice of metal-ion fluxes (Al^+ *vs*. Ti^+/Ti^{2+}) during hybrid HIPIMS/DCMS film growth, the chemical nature of the incident ion, inert gas *vs.* metal, can also play an important role in controlling nanostructural evolution. By applying substrate bias pulses only in synchronous with the metal-rich-plasma portion of the Al-HIPIMS pulse, such that ion irradiation of the growing film is predominantly by Al^+ ions, and comparing the results to film growth under continuous dc bias, the effects of gas *vs*. metal-ion irradiation on the properties of resulting $Ti_{0.39}Al_{0.61}N$ films were selectively probed. Switching from Ar^+ to Al^+ bombardment, while maintaining the same integrated incident ion/metal ratio, increases x_{max}, and hence film hardness, while decreasing intrinsic film growth stress even further.

The properties of HIPIMS/DCMS $Ti_{1-x}Al_xN$ films are governed by the average metal-ion momentum per deposited atom $\langle p_d \rangle$ transferred to the film surface with the critical value for maintaining single-phase cubic alloys ~135 $[\text{eV-amu}]^{1/2}$ for layers with $x \simeq 0.60$. Strong asymmetry in the flux of doubly-ionized metal-ions during HIPIMS operation with Al and Ti targets is decisive, and the critical $\langle p_d \rangle$ limit is easily exceeded in the case of Ti-HIPIMS, even with no intentional bias.

Pure HIPIMS deposition from segmented TiAl targets yields $Ti_{1-x}Al_xN$ films with high hardness for $x \leq 0.50$; however, the films also exhibit high compressive stress. At larger AlN concentrations, both H and σ decrease. The XRD kinetic solubility limit is higher than for Ti-HIPIMS/Al-DCMS alloys, but lower than for Al-HIPIMS/Ti-DCMS layers. These results provide independent evidence for the detrimental role of energetic doubly-ionized Ti^{2+} ions, present during Ti-HIPIMS operation, on film nanostructure and mechanical properties.

VIII. Acknowledgements

We thank Prof. Ivan Petrov for his enthusiasm and inspiration during this research and for valuable discussions. The financial support from the European Research Council (ERC) through an Advanced Grant and The VINN Excellence Center *Functional Nanoscale Materials (FunMat)* is gratefully acknowledged. We thank the staff at CemeCon AG and at the Tandem Laboratory, Uppsala University, for technical support.

Figure captions

Fig. 1. Ion energy distribution functions (IEDFs) from Al and Ti targets operated in both DCMS and HIPIMS modes. The DCMS data are time-averaged. For HIPIMS, the IEDFs correspond to the 20-μs highest-target-current-density portions of the 200 μs pulses. (Adapted from Ref. 40)

Fig. 2. Ti and Al fractions of doubly-charged metal-ions, $Me^{2+}/(Me^{2+}+Me^{+})$, detected at the substrate position as a function of peak target current density J_T during HIPIMS operation of Ti and Al targets in 1.0:0.2 Ar:N_2 gas mixtures at P_{tot} = 0.4 Pa (3 mTorr).

Fig. 3. θ–2θ scans as a function of tilt angle ψ for $Ti_{1-x}Al_xN$ alloy films with x = 0.59 grown on Si(001) at 500 °C by (a) Al-HIPIMS/Ti-DCMS, and (d) Ti-HIPIMS/Al-DCMS. (From Ref. 40). The peak labeled "S" in 3(a) at 2θ = 32.8°, with ψ = 0°, is the "forbidden" 002 reflection from the Si(001) substrate which appears due to multiple scattering.

Fig. 4. XTEM images, with corresponding selected area diffraction patterns as inserts, from $Ti_{1-x}Al_xN$ alloys grown on Si(001) at 500 °C with composition x: (a) x = 0.53, Ti-HIPIMS/Al-DCMS and (b) x = 0.59, Al-HIPIMS/Ti-DCMS. (From Ref.41)

Fig. 5. (a) Indentation hardness H and (b) residual stress σ (corrected for differential thermal contraction upon cooling the sample from T_s) of $Ti_{1-x}Al_xN$ films, grown on Si(001) at 500 °C using Al-HIPIMS/Ti-DCMS (filled squares) and Ti-HIPIMS/Al-DCMS (open circles) target configurations as a function of AlN concentration x. (Adapted from Ref. 40)

Fig. 6. Top-left panel: time evolution of the total flux of Ar^+, Al^+, N_2^+, and N^+ ions incident at the substrate during Al-HIPIMS/Ti-DCMS. Substrate bias V_s waveforms, together with XTEM images and SAED patterns (inserts) from corresponding $Ti_{0.39}Al_{0.61}N$ layers grown on Si(001) substrates at 500 °C, for: (a) continuous dc bias, (b) V_s applied in synchronous with the full HIPIMS pulse, and (c) V_s applied in synchronous with only the metal-rich-plasma portion of the HIPIMS pulse. (Adapted from Ref. 42)

Fig. 7. XTEM images, with corresponding SAED patterns, of (a) a $Ti_{0.38}Al_{0.62}N$ multilayer grown on Si(001) at 500 °C in the Al-HIPIMS/Ti-DCMS target configuration with V_s varied from 20 to 280 V for individual layers; (b) a $Ti_{0.42}Al_{0.58}N$ multilayer grown on Si(001) at 500 °C in the Ti-HIPIMS/Al-DCMS target configuration with V_s varied from 20 to 120 V for individual layers. (From Ref. 43)

Fig. 8 Average (a) ion energy $\langle E_d \rangle$ and (b) momentum $\langle p_d \rangle$, per deposited atom, incident at the film growth surface during deposition of $Ti_{1-x}Al_xN$ (x ~0.6) at 500 °C as a function of V_s. The films were grown on Si(001) substrates by Al-HIPIMS/Ti-DCMS (solid lines) and Ti-HIPIMS/Al-DCMS (dashed lines). (Adapted from Ref. 43)

Fig. 9. Time-averaged intensities of low-energy ion fluxes at the substrate position recorded from the $Ti_{30}Al_{70}$ alloy target during HIPIMS operation.

Fig. 10. θ–2θ scans as a function of tilt angle ψ for $Ti_{1-x}Al_xN$ alloy films with $x = 0.62$, grown on Si(001) at 500 °C from a segmented TiAl target.

Fig. 11. Relaxed lattice parameters a_o of $Ti_{1-x}Al_xN$ films grown on Si(001) at 500 °C plotted as a function of AlN concentration for three different target configurations: TiAl-HIPIMS (filled triangles), Al-HIPIMS/Ti-DCMS (filled squares), and Ti-HIPIMS/Al-DCMS (open circles).

REFERENCES

[1] U. Wahlström, L. Hultman, J.-E. Sundgren, F. Adibi, I. Petrov and J. E. Greene, Thin Solid Films 235 (1993) 62-70
[2] F. Adibi, I. Petrov, J.E. Greene, U. Wahlstrom, J.-E. Sundgren, J. Vac. Sci. Technol. A 11 (1993) 136
[3] A. Hörling, L. Hultman, M. Odén, J. Sjölén, L. Karlsson, J. Vac. Sci. Technol. A 20 (2002) 1815
[4] T. Ikeda, H. Satoh, Thin Solid Films 195 (1991) 99
[5] H. Oettel, R. Wiedemann, S. Preisler, Surf. Coat. Technol. 74-75 (1995) 273
[6] C.V. Falub, A. Karimi, M. Ante, W. Kalss, Surf. Coat. Technol. 201 (2007) 5891
[7] D.M. Mattox, G.J. Kominiak, J. Vac. Sci. Technol. 9 (1972) 528
[8] G. Hakansson, J.-E. Sundgren, D. McIntyre, J.E. Greene, W.-D. Munz, Thin Solid Films 153 (1987) 55
[9] T. C. Huang , G. Lim , F. Parmigiani and E. Kay, J. Vac. Sci. Technol. A 3 (1985) 2161
[10] J.L. Mukherjee, L.C. Wu, J.E. Greene, H.E. Cook, J. Vac. Sci. Technol. 12 (1975) 850
[11] L.C. Wu, J.E. Greene, J. Appl. Phys. 50 (1979) 4966
[12] J.S. Colligon, H. Kheyrandish, Vacuum 39 (1989) 705
[13] J.E. Pawel, C.J. McHargue, J.J. Wert, Nuclear Instruments & Methods in Physics Research B 46 (1990) 392
[14] N.-E. Lee, G.A. Tomasch, J.E. Greene, Applied Physics Letters 65 (1994) 3236
[15] L. Hultman, J.-E. Sundgren, J.E. Greene, D.B. Bergstrom, and I. Petrov, J. Appl. Phys. 78 (1995) 5395
[16] F. Adibi, I. Petrov, J.E. Greene, L. Hultman, and J.-E. Sundgren, J. Appl. Phys. 73 (1993) 8580
[17] I. Petrov, P.B. Barna, L. Hultman, and J.E. Greene, J. Vac. Sci. Technol. A 21 (2003) S117
[18] J.E. Greene, "Nucleation, Growth, and Microstructural Evolution in Films Grown by Physical Vapor Deposition," in *Deposition Technologies for Films and Coatings*, ed. by R.F. Bunshah, Noyes Publications, Park Ridge, NJ (1994), p. 681.
[19] J.E. Greene, "Thin Film Nucleation, Growth, and Microstructural Evolution: an Atomic Scale View," in *Handbook of Deposition Technologies for Thin Films and Coatings*, Third Edition, ed. by P. Martin, William Andrew Publications (Elsevier), Burlington, MA (2010).
[20] A.K. Agarwal, A. Garg, D.K. Srivastava, M. K. Shukl, Surf. Coat. Technol. 201 (2007) 6182
[21] J.S. Schuster and J. Bauer, J. Solid State Chem. 53 (1984) 260
[22] J.M.E. Harper, J.J. Cuomo, R. J. Gambino, and H. R. Kaufman, in Ion Bombardment Modification of Surfaces, edited by O. Auciello and R. Kelly (Elsevier, New York, 1984). Chap. 4.
[23] T. C. Huang, G. Lim, F. Parmigiani, and E. Kay, J. Vac. Sci. Technol. A 3 (1985) 2161
[24] V. Poulek, J. Musil, V. Valvoda, and R. Kuzel, Thin Solid Films 196 (1991) 265
[25] I. Petrov, F. Adibi, J.E. Greene, L. Hultman, and J.-E. Sundgren, Appl. Phys. Lett. 63 (1993) 36
[26] I. Petrov, F. Adibi, J.E. Greene, W.D. Sproul, and W.-D. Munz, J. Vac. Sci. Technol. A 10 (1992) 3283
[27] J. E. Greene, J.-E. Sundgren, L. Hultman, I. Petrov, and D. B. Bergstrom, Appl. Phys. Lett. 67 (1995) 2928
[28] C.-S. Shin, Y.-W. Kim, D. Gall, J. E. Greene, and I. Petrov, Thin Solid Films 402 (2002) 172
[29] D. Gall, C.-S. Shin, T. Spila, M. Odén, M. J. H. Senna, J. E. Greene, and I. Petrov, J. Appl. Phys. 91 (2002) 3589
[30] D. Gall, I. Petrov, N. Hellgren, L. Hultman, J.-E. Sundgren, and J. E. Greene, J. Appl. Phys. 84 (1998) 6034
[31] D. Gall, I. Petrov, and J. E. Greene, J. Appl. Phys., 89 (2001) 401
[32] I. Petrov, A. Myers, J. E. Greene, and J. R. Abelson, J. Vac. Sci. Technol. A, 12 (1994) 2846
[33] G. Greczynski, J. Jensen, L. Hultman, IEEE Transactions on Plasma Science 38 (2010) 3046
[34] P. Sigmund, J. Vac. Sci. Technol. A 17 (1979) 396-399
[35] J. T. Gudmundsson, Journal of Physics: Conference Series 100 (2008) 082013
[36] H. Windischmann, J. Vac. Sci. Technol. A 9 (1991) 2431
[37] D. J. Kester and R. Messier, J. Appl. Phys. 72 (1992) 504
[38] W. Otano-Rivera, L. J. Pilione, J. A. Zapien and R. Messier, J. Vac. Sci. Technol. A 16 (1998) 1331
[39] V. Kouznetsov, K. Macak, J.M. Schneider, U. Helmersson and I. Petrov, Surf. Coat. Technol. 122 (1999) 290
[40] G. Greczynski, J. Lu, M. Johansson, J. Jensen, I. Petrov, J.E. Greene, and L. Hultman, Surf. Coat. Technol. 206 (2012) 4202
[41] G. Greczynski, J. Lu, M. Johansson, J. Jensen, I. Petrov, J.E. Greene, and L. Hultman, Vacuum 86 (2012) 1036
[42] G. Greczynski, J. Lu, J. Jensen, I. Petrov, J.E. Greene, S. Bolz, W. Kölker, Ch. Schiffers, O. Lemmer and L. Hultman, J. Vac. Sci. .Technol. A 30 (2012) 061504-1

[43] G. Greczynski, J. Lu, J. Jensen, I. Petrov, J.E. Greene, S. Bolz, W. Kölker, Ch. Schiffers, O. Lemmer and L. Hultman, *Thin Solid Films,* accepted
[44] J. Böhlmark, J. Alami, C. Christou, A.P. Ehiasarian, U. Helmersson, J. Vac. Sci. Technol. A 23 (2005) 18
[45] K. Macak, V. Kouznetsov, J. Schneider, U. Helmersson and I.Petrov, J. Vac. Sci. Technol. A 18 (2000) 1533
[46] K. Bobzin, N. Bagcivan, P.Immich, S. Bolz, J. Alami and R. Cremer, J. Mat. Process. Technol. 209 (2009) 165
[47] Q. Luo, S. Yang, K.E. Cooke, Surf. Coat. Technol. 236 (2013) 13
[48] J. Paulitsch, M. Schenkel, Th. Zufras, P.H. Mayrhofer, W.-D. Munz, *Thin Solid Films* 518 (2010) 5558
[49] G. Greczynski and L. Hultman, Vacuum 84 (2010) 1159–1170
[50] David R. Lide (ed), *CRC Handbook of Chemistry and Physics, 84th Edition*. CRC Press. Boca Raton, Florida, 2003; Section 10, Atomic, Molecular, and Optical Physics; Ionization Potentials of Atoms and Atomic Ions.
[51] see, e.g., chapter 6 in M. Birkholz *Thin Film Analysis by X-ray Scattering*, ISBN-10: 3-527-31052-5, Wiley-VCH, Weinheim 2006
[52] The JCPDS database (1998), data set number: 38-1420; W. Wong-Ng, H. McMurdie, B. Paretzkin, C. Hubbard, A. Dragoo, Powder Diffraction 2 (1987) 2
[53] P.H. Mayrhofer, H. Clemens, C. Mitterer, Z. Metallk. 96 (2005) 468-80
[54] I. Petrov, L. Hultman, U. Helmersson, J.E. Sundgren, J.E. Greene, Thin Solid Films 169 (1989) 299
[55] S. M. Rossnagel, J. Vac. Sci. Technol. A 6 (1988) 19-24
[56] J.-S. Chun, I. Petrov, and J. E. Greene, J. Appl. Phys. 86 (1999) 3633
[57] A. Kimura, H. Hasegawa, K. Yamada, T. Suzuki, Surf. Coat. Technol. 120 (1999) 438
[58] K. Kutschej, P. H. Mayrhofer, M. Kathrein, P. Polcik, R. Tessadri, C. Mitterer, Surf. Coat. Technol. 200 (2005) 2358
[59] B. Alling, A. Karimi, I.A. Abrikosov, Surf. Coat. Technol. 203 (2008) 883
[60] We note that lower x_{max} values may be obtained by higher resolution techniques such as SAED.
[61] G. Greczynski, J. Jensen, L. Hultman, Thin Solid Films 519 (2011) 6354–6361
[62] A. Anders, J. Andersson, A. Ehiasarian, J. Appl. Phys. 102 (2007) 113303
[63] P. Kudláček, J. Vlček, K. Burcalová and J. Lukáš, Plasma Sources Sci. Technol. 17 (2008) 025010

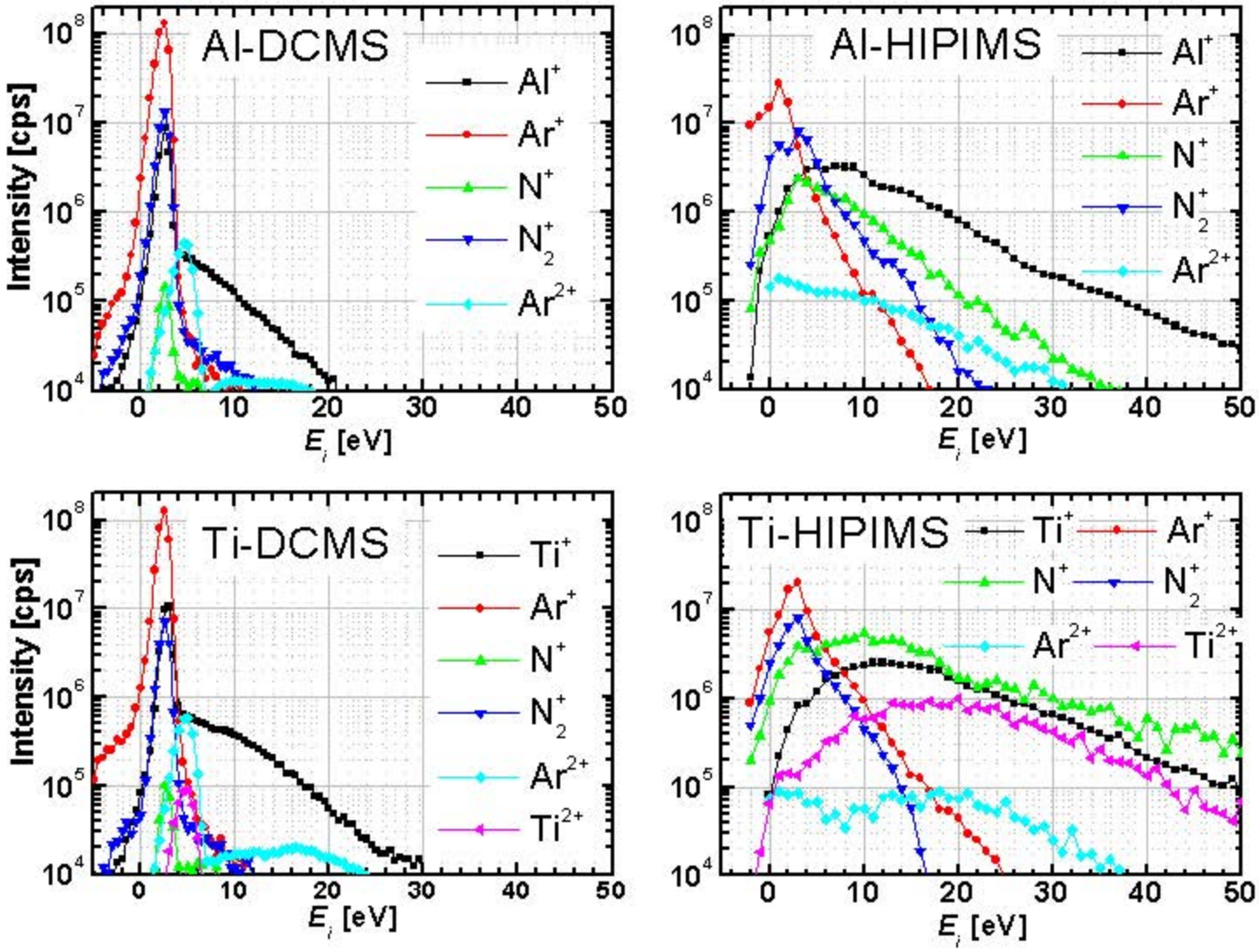
Al-DCMS
Al-HIPIMS
Ti-DCMS
Ti-HIPIMS
Intensity [cps]
E_i [eV]
Al^+
Ar^+
N^+
N_2^+
Ar^{2+}
Ti^+
Ti^{2+}

Fig. 1

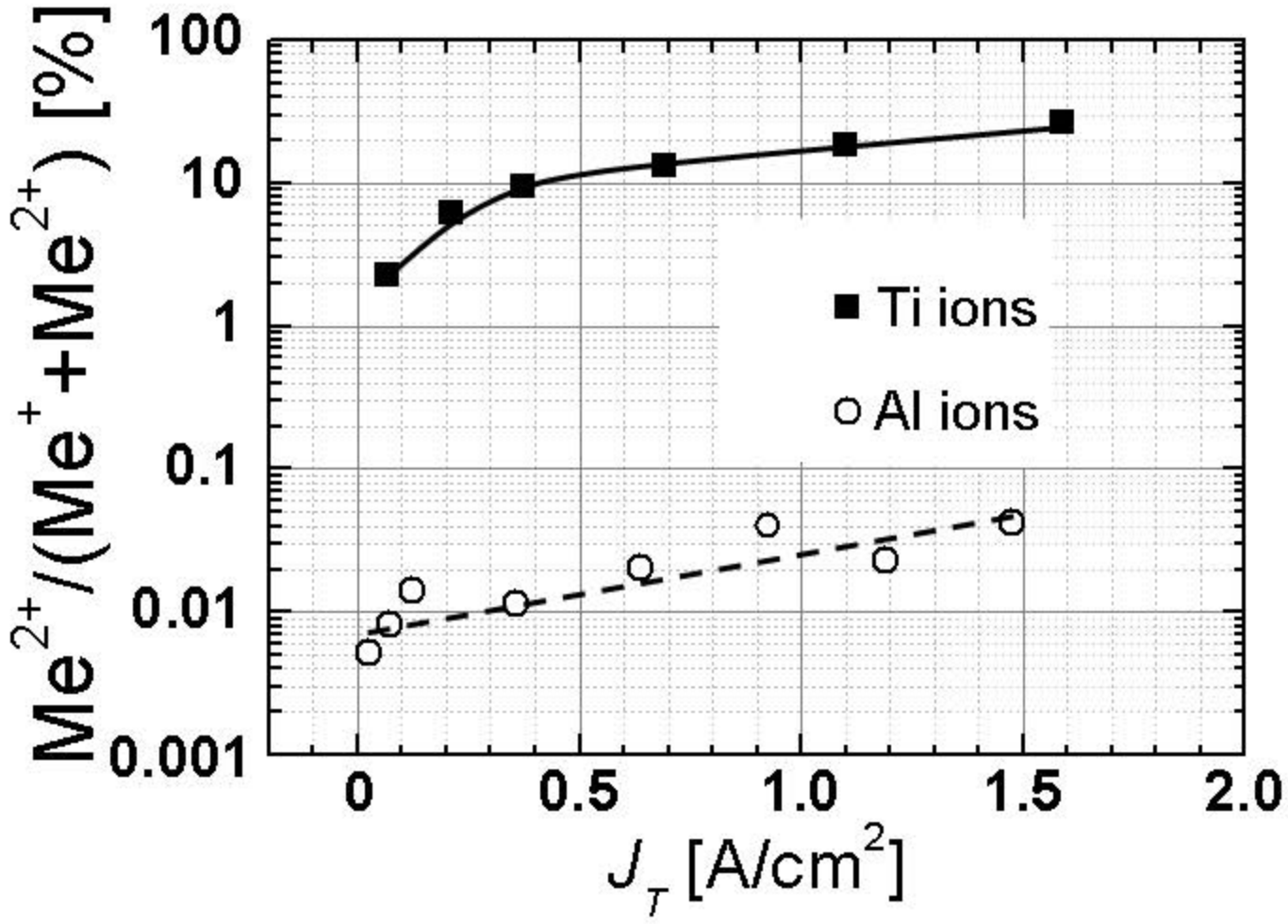
100
10
1
0.1
0.01
0.001
0
0.5
1.0
1.5
2.0
$Me^{2+}/(Me^{+}+Me^{2+})$ [%]
J_T [A/cm^2]
Ti ions
Al ions

Fig. 2

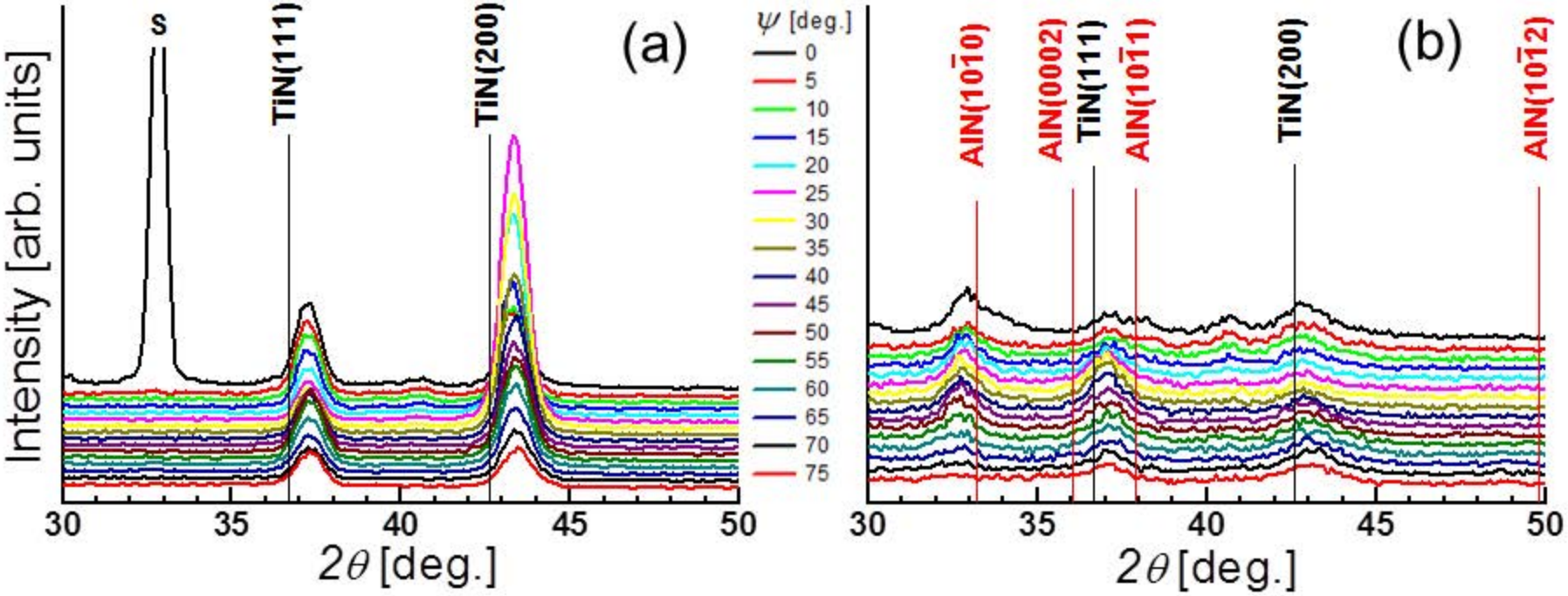
(a)
(b)
Intensity [arb. units]
2θ [deg.]
ψ [deg.]
0
5
10
15
20
25
30
35
40
45
50
55
60
65
70
75
S
TiN(111)
TiN(200)
AlN(10$\bar{1}$0)
AlN(0002)
TiN(111)
AlN(10$\bar{1}$1)
TiN(200)
AlN(10$\bar{1}$2)
30
35
40
45
50

Fig. 3

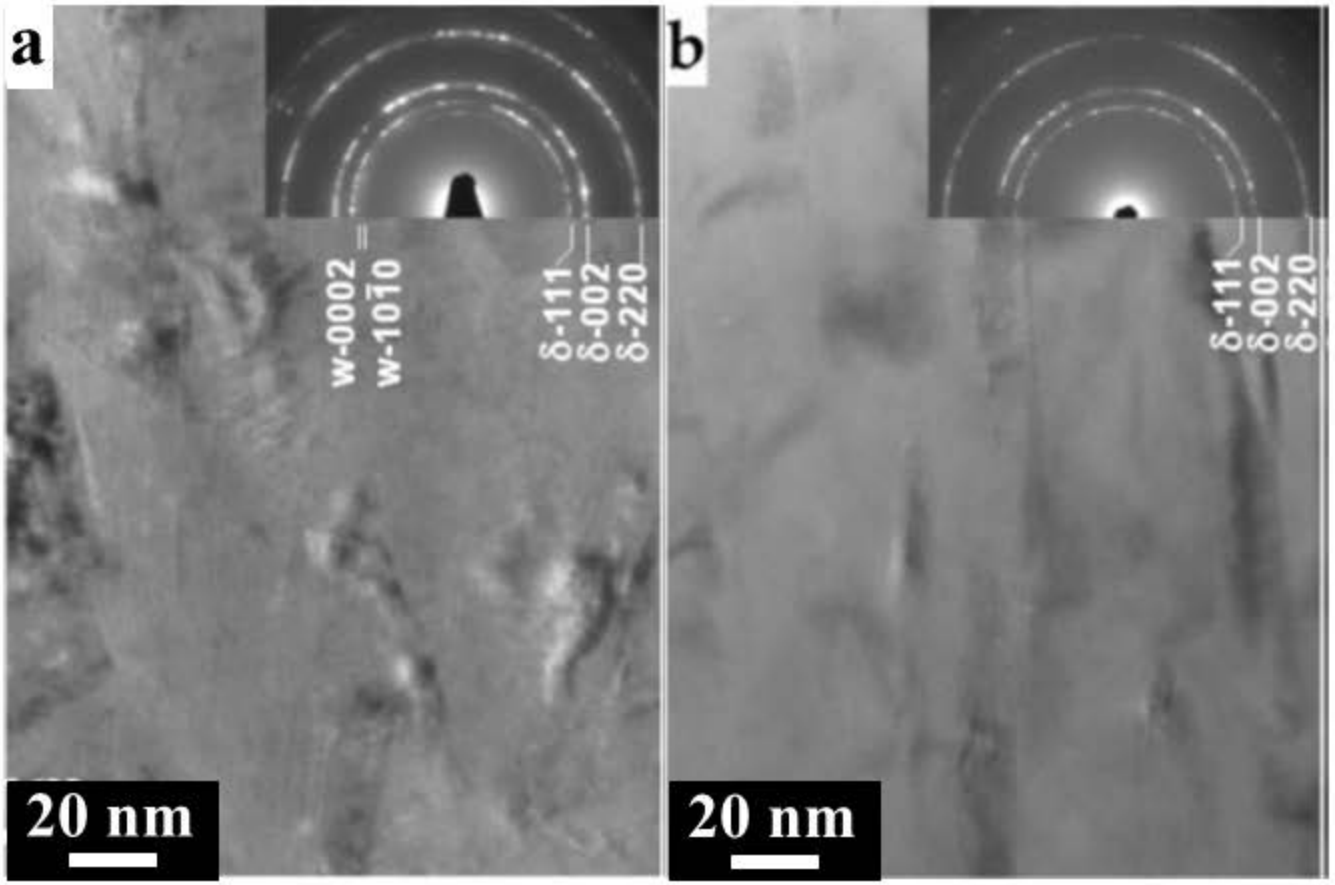

Fig. 4

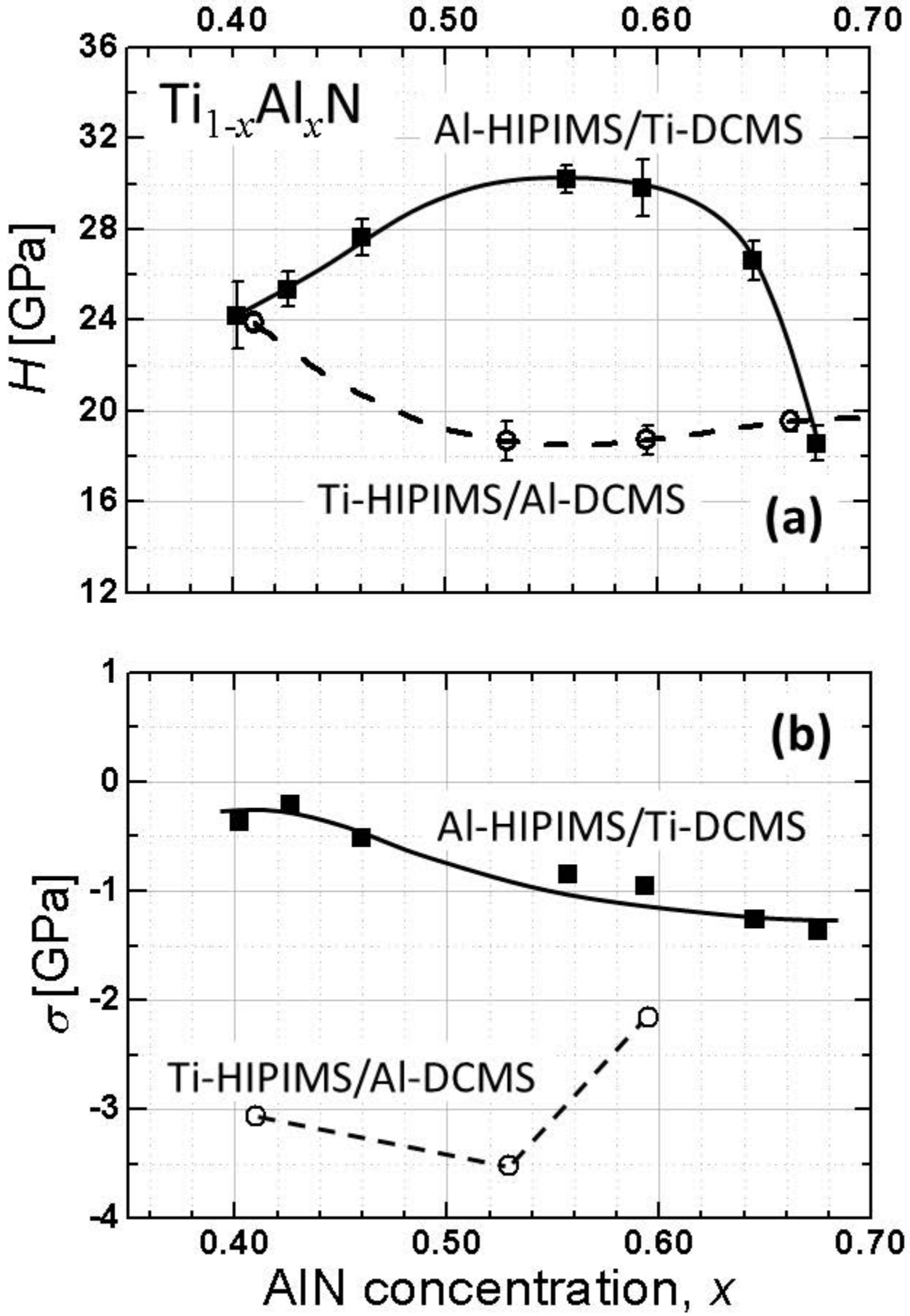
0.40
0.50
0.60
0.70
36
32
28
24
20
16
12
H [GPa]
Ti1-xAlxN
Al-HIPIMS/Ti-DCMS
Ti-HIPIMS/Al-DCMS
(a)
1
0
-1
-2
-3
-4
σ [GPa]
(b)
Al-HIPIMS/Ti-DCMS
Ti-HIPIMS/Al-DCMS
0.40
0.50
0.60
0.70
AlN concentration, x

Fig. 5

Fig. 6

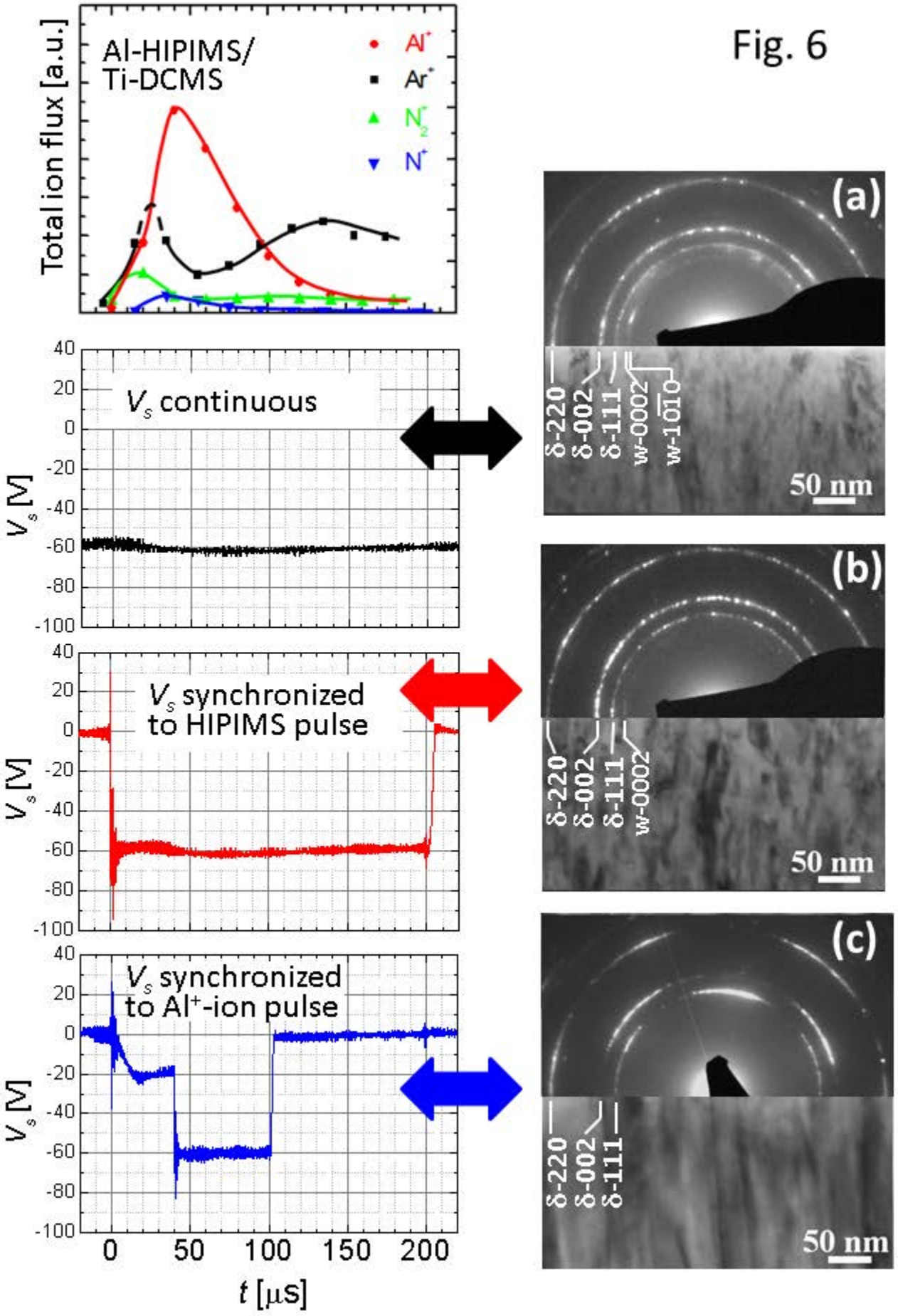
Total ion flux [a.u.]
Al-HIPIMS/
Ti-DCMS
Al+
Ar+
N2+
N+
Vs continuous
Vs synchronized
to HIPIMS pulse
Vs synchronized
to Al+-ion pulse
Vs [V]
t [μs]
(a)
(b)
(c)
δ-220
δ-002
δ-111
w-0002
w-1010
50 nm

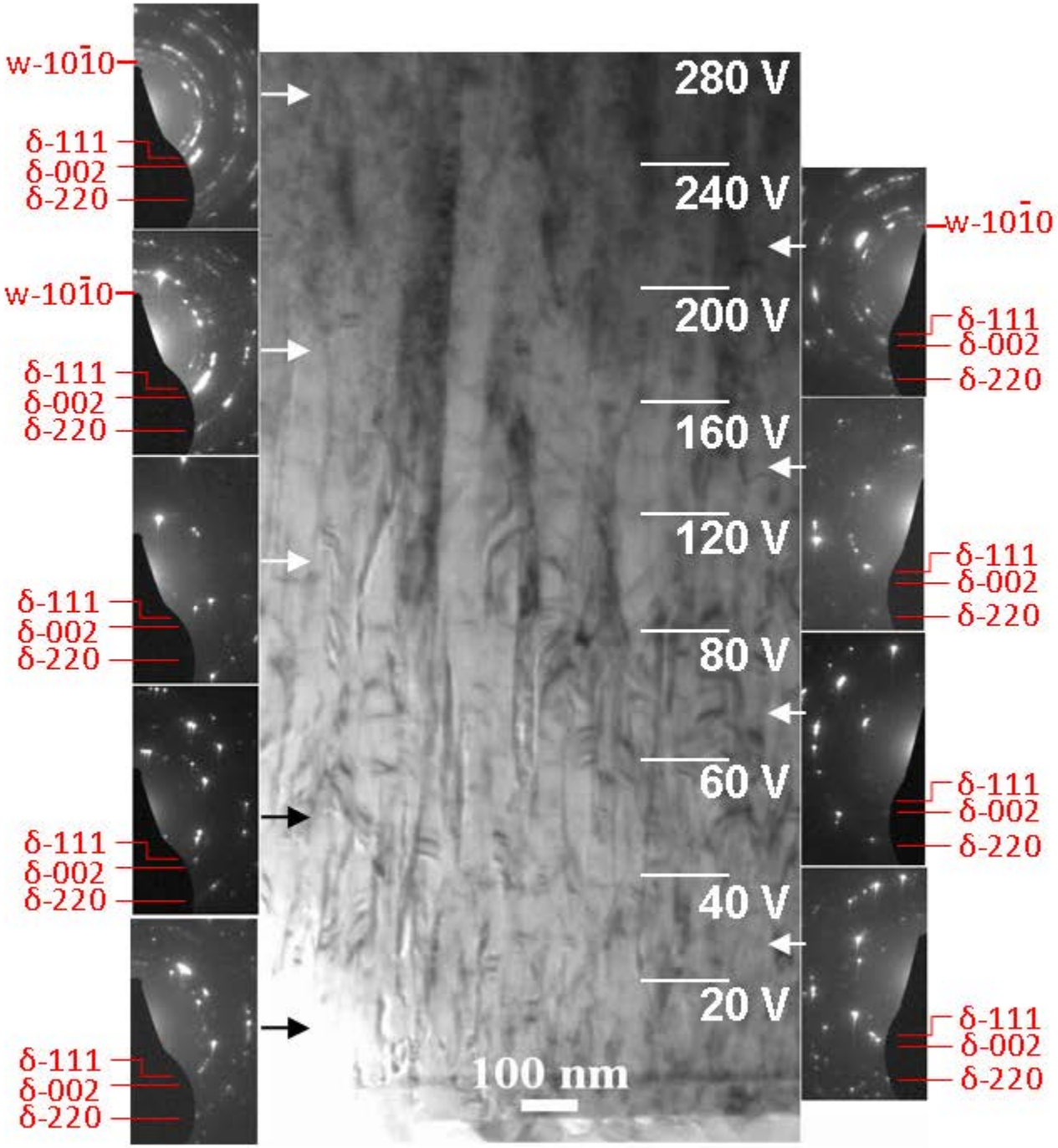
w-10$\bar{1}$0
δ-111
δ-002
δ-220
280 V
240 V
200 V
160 V
120 V
80 V
60 V
40 V
20 V
100 nm

Fig. 7(a)

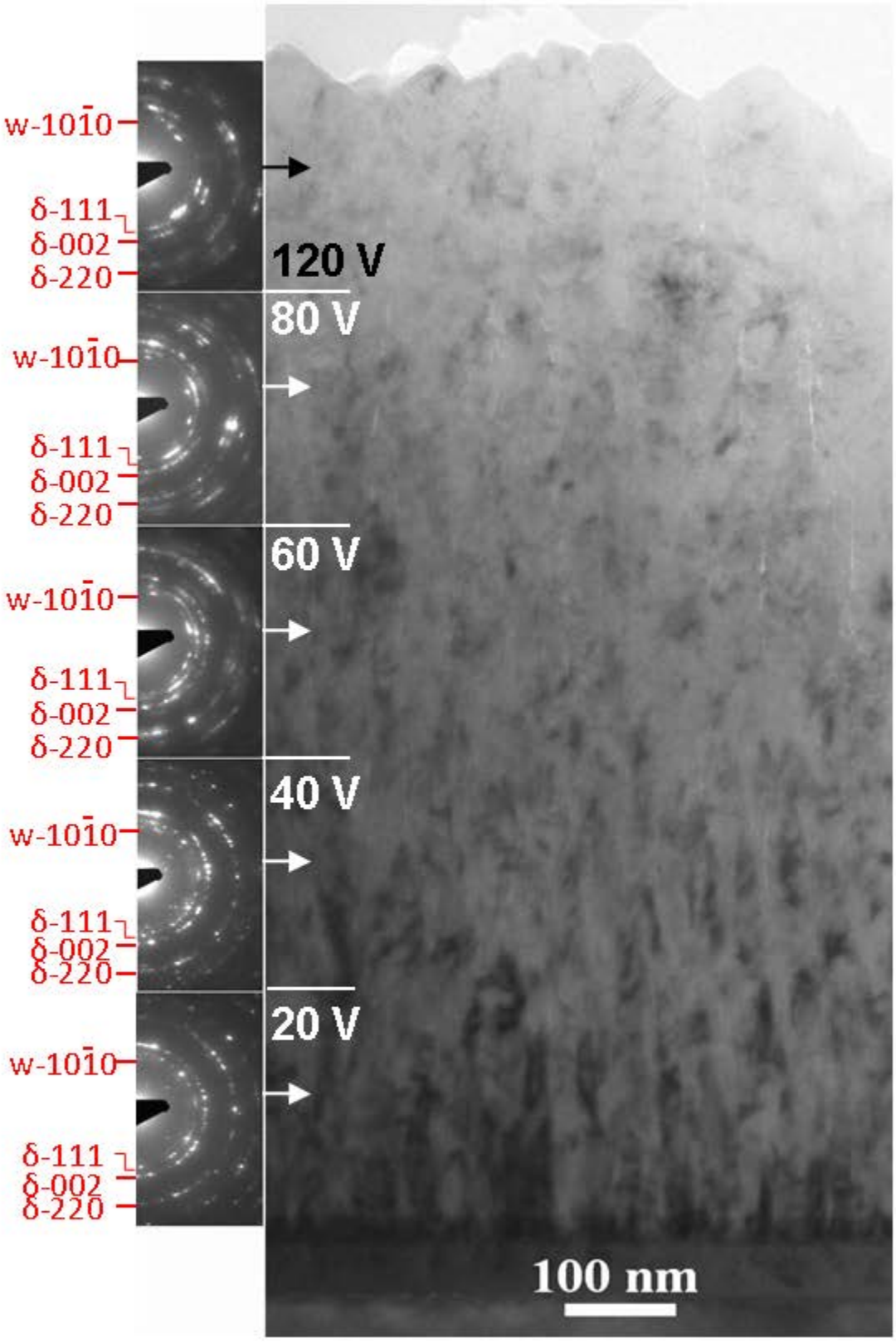

Fig. 7(b)

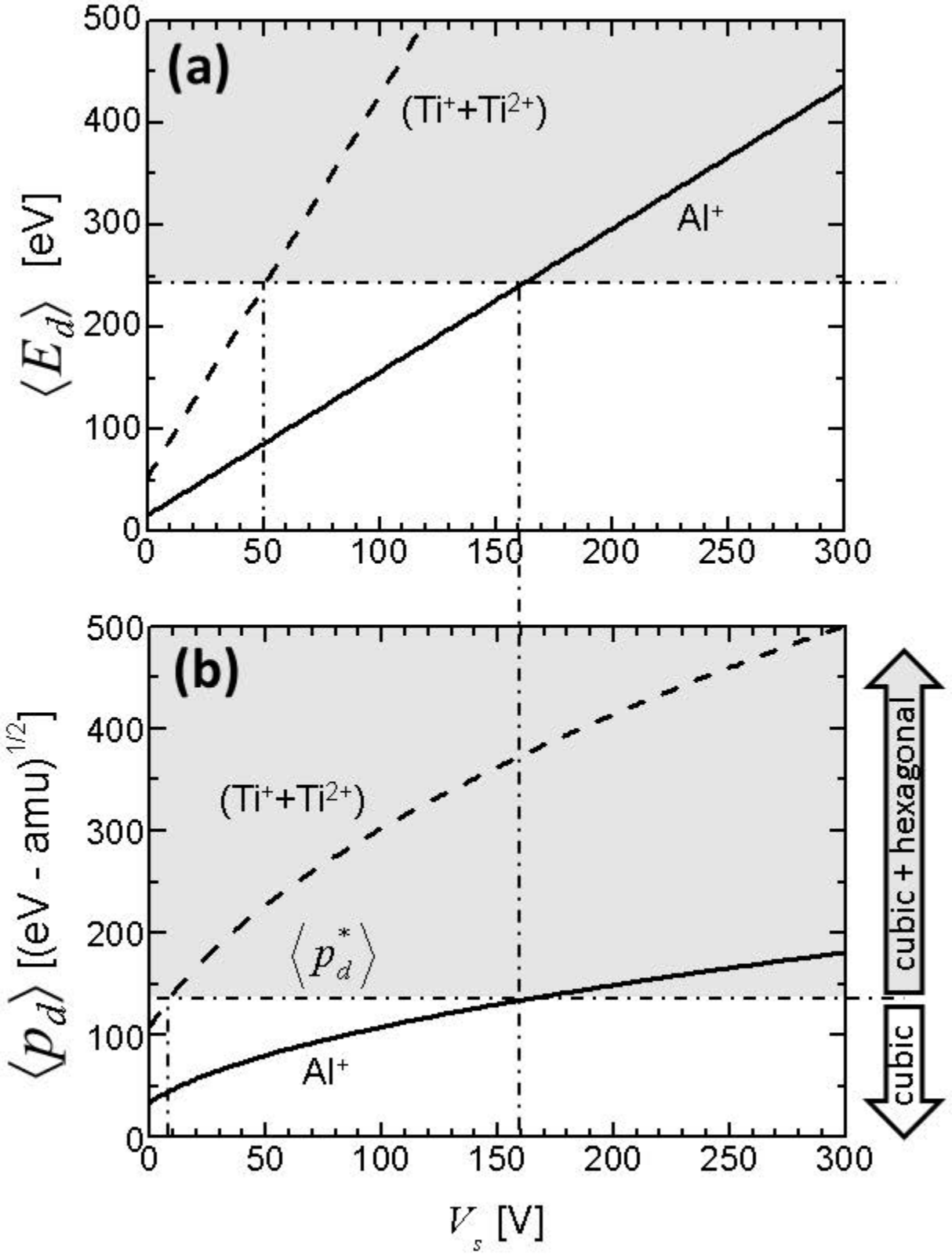
(a)
(Ti+ + Ti2+)
Al+
⟨Ed⟩ [eV]
0
100
200
300
400
500
0
50
100
150
200
250
300
(b)
(Ti+ + Ti2+)
⟨p*d⟩
Al+
⟨pd⟩ [(eV - amu)1/2]
cubic + hexagonal
cubic
Vs [V]

Fig. 8

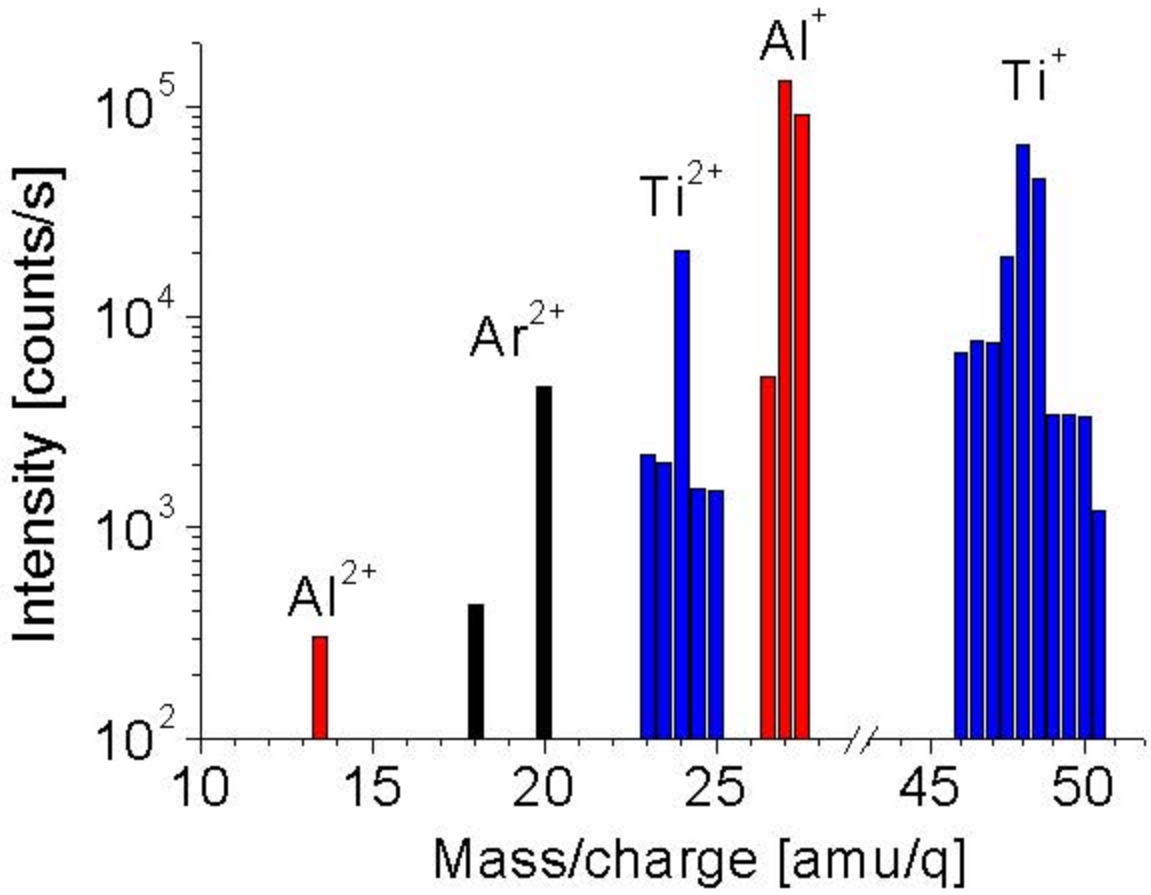
Intensity [counts/s]
10^5
10^4
10^3
10^2
Al^2+
Ar^2+
Ti^2+
Al^+
Ti^+
10
15
20
25
45
50
Mass/charge [amu/q]

Fig. 9

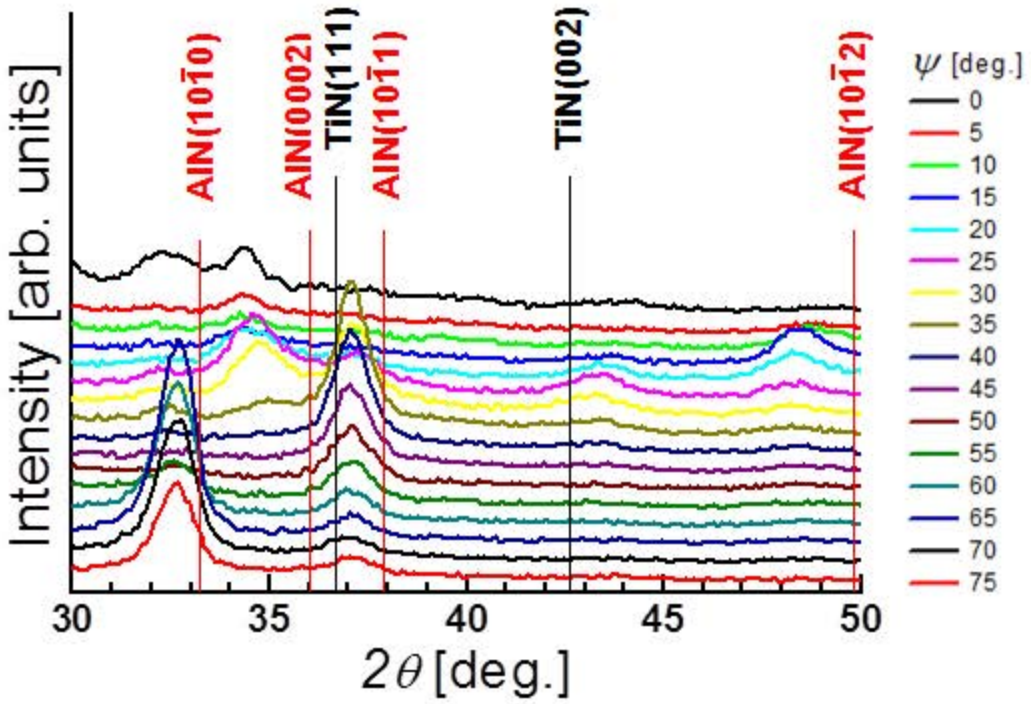
Intensity [arb. units]
AlN(10$\bar{1}$0)
AlN(0002)
TiN(111)
AlN(10$\bar{1}$1)
TiN(002)
AlN(10$\bar{1}$2)
ψ [deg.]
0
5
10
15
20
25
30
35
40
45
50
55
60
65
70
75
30
35
40
45
50
2θ [deg.]

Fig. 10

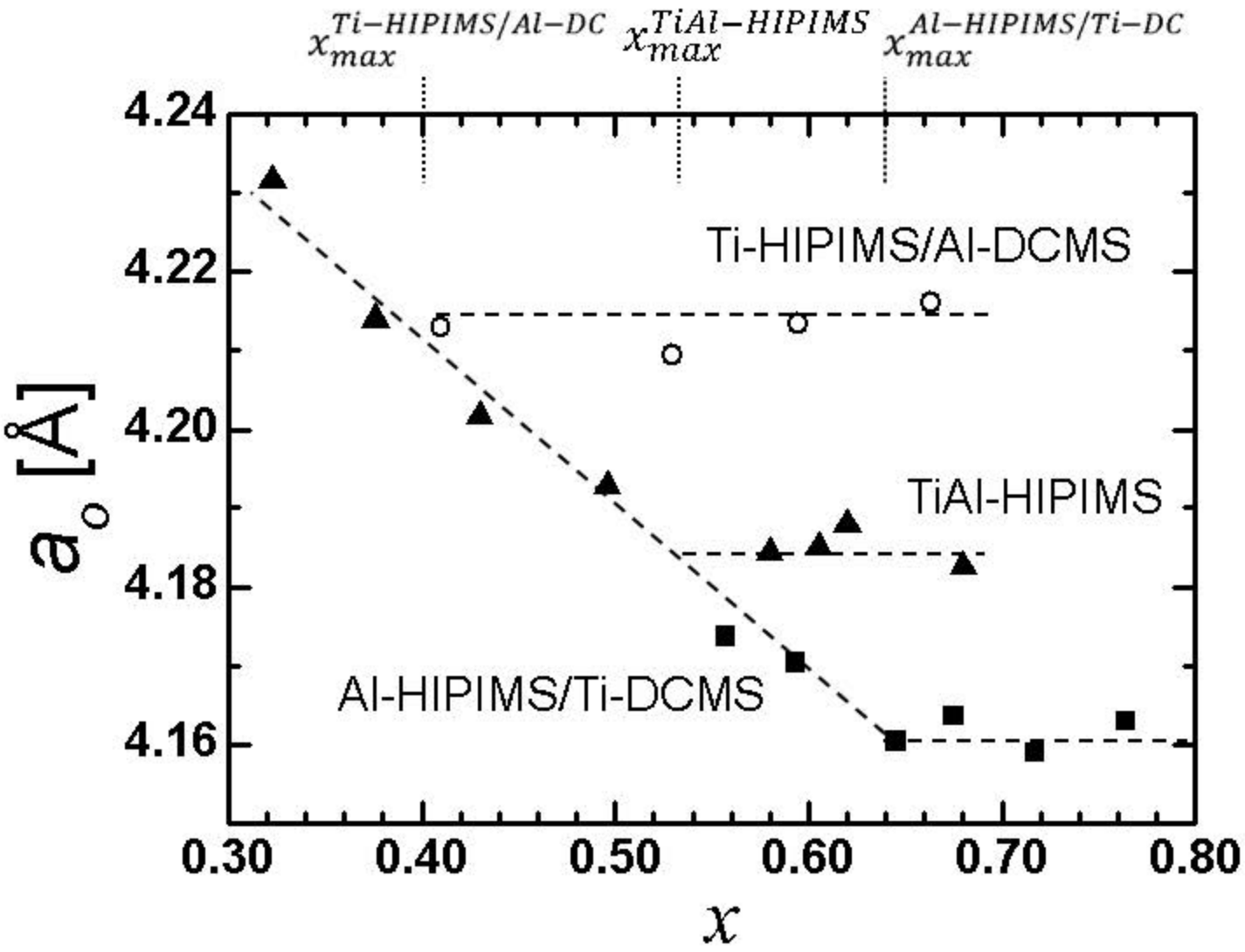
$x_{max}^{Ti-HIPIMS/Al-DC}$
$x_{max}^{TiAl-HIPIMS}$
$x_{max}^{Al-HIPIMS/Ti-DC}$
Ti-HIPIMS/Al-DCMS
TiAl-HIPIMS
Al-HIPIMS/Ti-DCMS
a_o [Å]
4.24
4.22
4.20
4.18
4.16
0.30
0.40
0.50
0.60
0.70
0.80
x

Fig. 11